Physics of Plasmas

Azimuthal structures and turbulent transport in Penning discharge

Cite as: Phys. Plasmas **30**, 033506 (2023); https://doi.org/10.1063/5.0129804
Submitted: 07 October 2022 • Accepted: 22 January 2023 • Published Online: 01 March 2023

M. Tyushev, M. Papahn Zadeh, V. Sharma, et al.

Physics of Plasmas ARTICLE scitation.org/journal/php

Azimuthal structures and turbulent transport in Penning discharge

Cite as: Phys. Plasmas **30**, 033506 (2023); doi: 10.1063/5.0129804
Submitted: 7 October 2022 · Accepted: 22 January 2023 ·
Published Online: 1 March 2023

M. Tyushev,[1,a)] M. Papahn Zadeh,[1] V. Sharma,[1] M. Sengupta,[1] Y. Raitses,[2] J.-P. Boeuf,[3] and A. Smolyakov[1]

AFFILIATIONS

[1]Department of Physics and Engineering Physics, University of Saskatchewan, Saskatoon, Saskatchewan S7N 5E2, Canada
[2]Princeton Plasma Physics Laboratory, Princeton, New Jersey 08540, USA
[3]LAPLACE, Université de Toulouse, CNRS, INPT, UPS, 118 Route de Narbonne, 31062 Toulouse, France

[a)]Author to whom correspondence should be addressed: mikhail.tyushev@usask.ca

ABSTRACT

Azimuthal structures in cylindrical Penning discharge are studied with a 2D3V radial–azimuthal PIC/MCC model with the axial magnetic field. The discharge is self-consistently supported by ionization due to the axial injection of electrons. It is shown that the steady-state discharge can be supported in two different regimes with different types of observed azimuthal structures. The transition between the regimes is controlled by the mechanism of the energy input to the discharge. In the first regime (low energy of the injected electrons), with the pronounced $m = 1$ spoke activity, the power input is dominated by the energy absorption due to the radial current and self-consistent electric field. In the other regime (higher energy of the injected electrons), with prevalent small-scale $m > 1$ spiral structures, and the lower values of the anomalous transport, the total energy deposited to the discharge is lower and is mostly due to the direct input of the kinetic energy from the axial electron beam. We show that the large ($m = 1$) spoke and small-scale structures occur as a result of Simon–Hoh and lower hybrid instabilities driven by the electric field, density gradient, and collisions.

I. INTRODUCTION

Magnetically enhanced plasma discharges are widely used in industry and various technologies. The regime of partially magnetized plasmas, when the electrons are magnetized and strongly confined by the magnetic field, while the ions are weakly magnetized and can be controlled via the electric field, offers many opportunities for various applications for high density plasmas. At the same time, however, a combination of the magnetic field and plasma gradients results in the appearance of drift waves, instabilities, and turbulence. Plasma and energy transport across the magnetic field due to turbulent fluctuations and large-scale structures are typically much larger than the classical values. Despite the wide usage of magnetically enhanced plasma sources in the industry and the long history of studies, the physics of fluctuations and anomalous transport in such devices is still poorly understood impeding the further progress and development of new applications.

A plasma cylinder with an axial magnetic field is a prototype configuration for the Penning discharges used in many technological applications. In this paper, we study fluctuations and nonlinear structures in the cylindrical partially magnetized $\mathbf{E} \times \mathbf{B}$ Penning plasma discharge using a 2D radial–azimuthal PIC-MCC model. The goal of the study is to clarify the mechanisms and characteristics of instabilities and transport in this system. Our study emphasizes the role of self-consistent ionization as well as the physics of large- (spokes) and small-scale (spiral arms) azimuthal structures that appear in the nonlinear saturated state.

We focus on the case when the discharge is self-consistently sustained by the energy input from the axially injected electrons representing the electron beam from the RF cathode of the Penning discharge device.[1,2] We demonstrate that in addition to the direct kinetic energy of the electron beam, the energy absorption due to the radial electron current and the radial electric field is an important mechanism of the power input to the discharge. The total power delivered to the discharge and relative contributions of these two mechanisms define what type of azimuthal structures is excited in the discharge.

The potential in the discharge center is negative with respect to the walls due to the injection of beam electrons in this region. The potential drop depends on the current and energy of the beam electrons and is larger for lower beam energy because of the more efficient

electron trapping by the magnetic field. Therefore, for lower beam electron energy, electron energy absorption is dominated by the radial current and self-consistent radial electric field. In these conditions, the simulations show that large-scale structures, $m = 1$ spokes are excited. As the beam energy is increased, the potential drop is smaller, and the energy input becomes higher due to the direct kinetic energy from the axial electron beam. In that case, the small-scale spiral structures, with $m > 1$, dominate. We show that the large- and small-scale structures occur as a result of Simon–Hoh and lower hybrid type instabilities driven by the electric field, density gradient, and collisions.[3]

In Sec. II, the simulation model and main parameters are described. In Sec. III, we investigate the role of collisions and ionization on the development and saturation of the self-consistent discharge and present the benchmark simulations with four different PIC codes. The detailed study of the characteristics of azimuthal structures and their relation to gradient-drift instabilities is presented in Sec. IV. The parametric dependencies of spoke frequency on the magnetic field, box size, and ion species are studied in Sec. V. The regime with small-scale spiral arms is demonstrated and analyzed in Sec. VI. Section VII presents the comparison of anomalous transport between two regimes. A summary and discussion of the results are provided in Sec. VIII.

II. THE SIMULATION MODEL

In various applications with axial magnetic field both cylinder and rectangular cross section, configurations are used.[4–9] We employ the rectangular geometry of the discharge, as shown in Fig. 1, as our base case. We also study the effect of the geometry and provide a basic comparison of the result for the rectangular, dodecagon, and cylindrical models in Appendix B.

The simulations are performed on a uniform Cartesian grid in the x–y plane, with particles velocities in 3D $x - y - z$ space. A uniform axial magnetic field in the z-direction is applied perpendicular to the simulation domain with conducting Dirichlet boundary condition for the potential, $\Phi = 0$, and absorption for all incoming particles.

A uniform electron beam is injected axially inside a square region in the center ($0.6 \times 0.6\,\mathrm{cm}^2$). The density of the background neutral gas is uniform and constant throughout the simulations. The electron beam is represented by macro-particles introduced at every simulation time step. The beam electrons are injected with the same axial energy and zero temperature (zero energy spread) throughout the whole simulation.

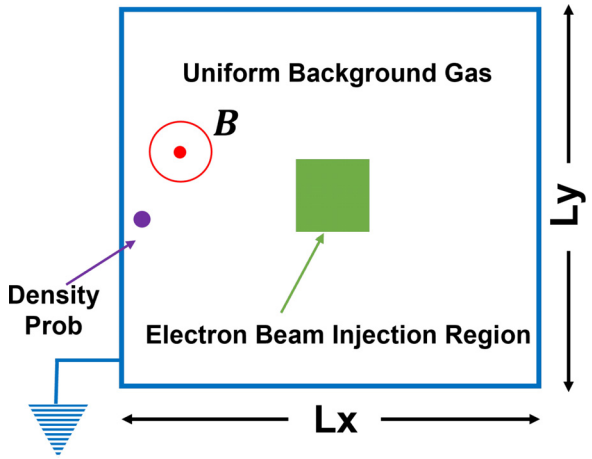

FIG. 1. The end view of the cross-section of the modeled discharge.

The simulations domain $L_x = L_y = 3\,\mathrm{cm}$ is split into $n_x \times n_y = 250 \times 250$ grid cells in the x- and y-directions. A typical injection region is a 50×50 cells square domain in the center of the box. This implies mesh resolution $\Delta x = 0.12\,\mathrm{mm}$ resolves Debye length through the simulations, which has been confirmed by the direct calculation of electron temperature and plasma concentration in each cell. The Debye length reaches its minimum in the center where it is equal to mesh resolution Δx.

The simulation time step is $\Delta t = 5\,\mathrm{ps}$ that resolves the electron cyclotron period and local plasma oscillation period by providing the practical criteria of $\omega_{pe,ce}\Delta t < 0.5$. Electron cyclotron frequency is $\omega_{ce} = 2.6 \times 10^9\,\mathrm{s}^{-1}$, and the characteristic value of plasma frequency is $\omega_{pe} = 5.6 \times 10^9\,\mathrm{s}^{-1}$ for $n_p = 10^{16}\,\mathrm{m}^{-3}$. The spatial grid and time step are set in a way that the Courant–Friedrichs–Lewy (CFL) condition is satisfied with a large margin. For the fastest particles, for which velocity is approximately equal to $2.4 \times 10^6\,\mathrm{m/s}$, we have $\mathrm{CFL} = v\Delta t/\Delta x = 0.1 \ll 1$. The weight of a single macro-particle was equivalent to $1.7 \times 10^7\,\mathrm{m}^{-1}$ for simulations with Argon gas, and for convergence study with Hydrogen gas, the number was $3 \times 10^6\,\mathrm{m}^{-1}$, both for electrons and ions since on average plasma is quasineutral. This value results in a low number of particles per cell (ppc) roughly equal to 3 (on average). Further simulations in $6 \times 6\,\mathrm{cm}^2$ geometry were performed with a higher ppc number, demonstrating good convergence as it is described in Secs. IV and VI. The change from 3×3 to $6 \times 6\,\mathrm{cm}^2$ box size was also motivated by the fact that the spoke structure that appears in our simulations has a characteristic length close to 3 cm. Therefore, to have a better view of the structure and lessen the role of boundaries, we increased the simulation domain. Nevertheless, the results of $3 \times 3\,\mathrm{cm}^2$ are used to show the convergence of global characteristics between different codes and also to show that, in this case, even the low resolution simulations capture essential dynamics.

In simulations, the electrons are magnetized, with small Larmor radius $\rho_e \ll L_x$, while ions remain unmagnetized (with Larmor radius much larger than plasma dimension $\rho_i \gg L_x$). We have tested the case of $3 \times 3\,\mathrm{cm}^2$ box with a magnetic field included in equations of motion for ions. Comparison with the case of unmagnetized ions showed that the effect is insignificant. Therefore, for simulations with the $6 \times 6\,\mathrm{cm}^2$ box, the magnetic field for ions was omitted.

The main plasma parameters for our base case are given in Table I. This is the regime when the large-scale $m = 1$ spoke structures

TABLE I. Physical parameters for the base case (spoke regime) simulations with Argon.

Property	Symbol	Value
Magnetic field	B(T)	0.015
Electron beam energy	E_b(eV)	1.84
Electron beam current	I_e(A/m)	0.544
Neutral temperature	T_n(K)	300
Neutral pressure	P_n(mTorr)	40
Neutral density	$n_n(\mathrm{m}^{-3})$	1.2875×10^{21}

are excited. The spoke regime is studied in Secs. III–V. It is important to note that in this case, the energy of injected electrons is low compared to ionization energy, and the ionization occurs mainly through electrons heated by the power deposited in the radial electron current and electric field via the axial electron current. In the regimes with the higher energy of the injected electrons, when the ionization occurs directly from the injected electrons, small-scale $m > 1$ spiral arm structures dominate as discussed in Sec. VI.

Our goal is to have a stationary discharge that is self-consistently maintained by the electron beam. As expected, ionization and collisions significantly affect the discharge characteristics, such as plasma density and fluctuations in energy in saturated steady-state. We consider and compare the discharge evolution and saturation for two scenarios: the case when only ionizing electron-neutral collisions, and the case when the ionization, elastic, and excitation processes in electron-neutral collisions are all included. The role of ionization and electron neutral collision was studied for two different neutral gases, Argon and Hydrogen. The details of these investigations are presented in Sec. III.

In this study, we omit ion-neutral collisions. The purpose of this work is to describe, using a 2D PIC-MCC kinetic model, the different types of instabilities likely to develop in a Penning-type source and to interpret them using theoretical dispersion relations. For this purpose, the physics of the problem has been simplified along these lines: (1) All ions created by ionization are assumed to reach the grounded electrode moving radially. In a real Penning source, a fraction of the ions created by ionization is lost in the axial direction (typically on the cathode side) along the z axis of our simulation domain. Since we do not simulate the z-direction in our simulations, such axial losses are not included. The assumption that all the ions are collected radially by the grounded electrode would be a good approximation for a very long (with respect to Lx and Ly) discharge in the z-direction. In principle, the axial losses could be simulated in 2D geometry by removing ions with some prescribed rate, but it was not done in the present manuscript. (2) We assume collisionless ions. This is not realistic for a 40 mTorr discharge but allows a direct comparison with results with dispersion relations with collisionless ions. We have actually found that the inclusion of ion collisions leads to more complex discharge regimes and instabilities and higher plasma density in the center of axial ion losses is not included. The resulting increase in plasma density goes beyond the values practical for available simulation resources. In this preliminary study, we have neglected the axial losses and ion collisions and leave the study of these effects (and methods to represent in a 2D model the boundary conditions along the z axis) to further work.

III. THE ROLE OF IONIZATION AND COLLISIONS FOR THE DISCHARGE SELF-SUSTAINMENT

One of the goals of this study was to study the large-scale spoke instability in the discharge with self-consistent ionization. It was found that parameters of the discharge, in particular, plasma density and fluctuation energy at saturation are rather sensitive to collision effects. We have employed several independent PIC-MCC codes to investigate the sources of the sensitivity and raise confidence in the results of the simulations. Descriptions of the codes used in this study are given in Appendix A. Though all codes follow general PIC-MCC methodology,[10] there are differences in Poisson solvers and the way particle collisions are implemented. This convergence study reveals that although all codes demonstrate qualitatively similar results, there are some quantitative differences. In particular, we find that the implementation of the collision algorithm is a source of some differences.

For the convergence studies, two parameters—the total number of physical particles and electrostatic energy—were used as a metric for the comparison between four codes. We use prevalent electron-neutral collisions: ionization, elastic, and excitation. Two cases were compared: the case with only ionizing collisions, and with ionizing and non-ionizing electron-neutrals collisions. As it was noted above, the ion-neutral collisions were omitted.

For our base case, we consider the situation when the axial energy of injected electrons is below the ionization threshold. We show that the electrons gain energy through the work of the radial electric current, so they are heated to initiate the discharge and support ionization. The axial electron current is maintained constant. The stationary values of plasma density and radial electric field in the discharge are established self-consistently by the balance of the input energy against ionization and losses through the boundaries. We inject electrons with equal energy and zero thermal velocity. In the regime when the most power to the discharge is delivered by the electric field, it is even possible to maintain the discharge with the injection of cold electrons. As long as the injected current remains the same, the characteristics of the discharge do not change much. The convergence of the discharge to the saturated state was confirmed with all four codes. As will be discussed in Sec. VI, the transition to a different regime occurs when the injected current is reduced while the beam kinetic energy is increased, so the ionization is maintained directly by the energetic electrons of the beam rather than by the electrons heated in the discharge.

Figure 2(a) shows the time evolution of total electron and ion inventories in Argon discharge simulated with only ionizing collisions. All but XOOPIC codes show a typical overshoot at the initial stage. The overshot recovers roughly by $t \simeq 10\,\mu$s, and all codes reach a steady state (after around $10\,\mu$s). The number of electrons and ions are close to each other, confirming quasi-neutrality in the simulations, except early stage between $t = 0.1$ and $t = 0.5\,\mu$s when the number of ions exceeds the number of electrons, due to electrons reaching the boundaries and being lost faster. In these simulations, the observed difference between the results of VSim, PEC2PIC, XOOPIC, and EDIPIC-2D was about 10% or less when the same number of particles per cell is used. The case for EDIPIC with high ppc differs more, which invalidates the data to study the processes. However, it still fulfills the purpose of the benchmark, and it will not be used further down the article.

Figure 2(b) shows the time evolution of particles inventory in the Argon discharge simulations with ionizing and non-ionizing electron neutral collisions included. In this case, the number of particles increases initially and reach a steady state for all simulations codes (except VSim) around $10\,\mu$s. The discrepancy between the results of VSim with EDIPIC and EDIPIC with PEC2PIC at $t = 30\,\mu$s in Fig. 2(b) is almost 17%. The behavior of plasma density in VSim and XOOPIC codes suggests that the saturation in these runs is slower and will be reached at later times. To confirm this, we have performed simulations for Hydrogen. As it is shown in Figs. 5(a) and 5(b), the Hydrogen runs show good convergence for the total number of particles and electrostatic energy of fluctuations for all codes.

The evolution of the electrostatic energy (ES energy, $0.5\int_V E^2\,dV$, $V = 3 \times 3 \times 100\,\text{cm}^3$) is shown in Figs. 3(a) and 3(b) for both cases:

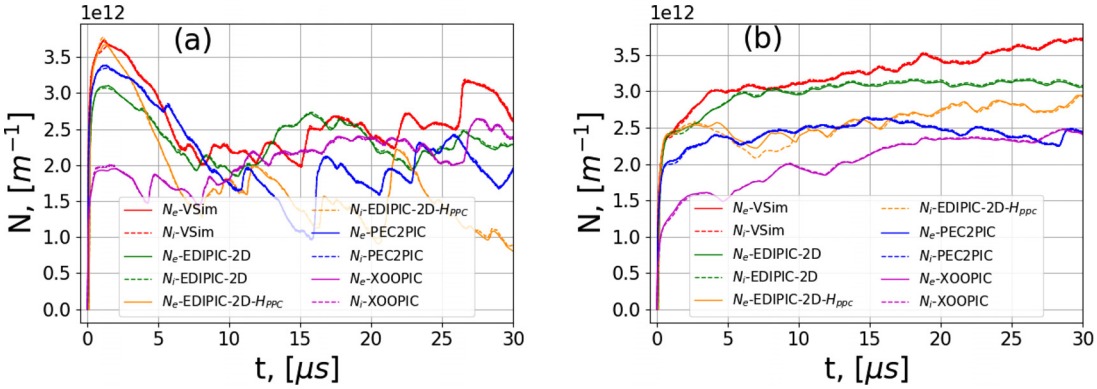

FIG. 2. Total particles inventory as a function of time: (a) case with only ionizing collision, (b) case with ionization and non-ionizing electron neutral collisions. The results from different codes are shown by different colors; solid lines show electrons and dashed lines—ions. The data with a H_{ppc} label is from the simulations with a larger number of computational particles per cell (ppc), which is around 85 for case (a) and 127 for case (b).

with ionization only and with ionizing and non-ionizing collisions. One can see that the saturation level of ES energy in simulation with only ionization collision is higher than for the case with ionization and non-ionizing electron neutral collisions.

Discrepancies in the results of presented simulations are believed to be due to the different ways the scattering cross-sectional data are imported and interpolated. We performed two simulations in VSim to compare the results of two ways the cross sections are evaluated: one where the scattering cross sections are imported from an open-access database LXcat and when the fitting function for the cross sections is used. The yellow lines in both Figs. 4(a) and 4(b) show the evolution of particles inventory for the VSim simulations with the cross-section fitting function. The results show a good agreement between VSim and PEC2PIC when both use the same MCC-cross-section fit. Relevant details of the cross-sectional data and references are given in Appendix A.

To further confirm that different methods of importing the cross-sectional data lead to some discrepancies, we have conducted an experiment with Hydrogen as the neutral gas and used the linear interpolation between two points. The value of cross-section for electron energy W is determined as $\sigma = (\sigma_{\text{left}}[W - W_l] + \sigma_{\text{left}}[W_r - W])/(W_r - W_l)$, where indexes r and l mean right and left data node correspondingly, between which the energy W of an electron is located. The result presented in Figs. 5(a) and 5(b) shows that all four codes give very similar results in the saturated state. The discrepancies at earlier times (<3 ms) are explained based on the different behavior of Poisson solvers for unresolved Debye length in the center and the artificial heating at this stage. At later stages, the density drops, and the Debye length is well resolved across the whole simulation box.

To investigate the role of ionization and collisions on the mode frequencies, we show in Fig. 6 the rotation frequency of the spoke from PEC2PIC simulations measured using Fast-Fourier-Transform (FFT) of a density probe's signal. The density probe measures local fluctuations in ion and electron densities at a location 0.084 cm inside the left wall, i.e., a distance of $0.028L_x$ from the left wall, and a distance of 1.44 cm from the bottom wall, i.e., a height of $0.48L_y$ referencing Fig. 1. The probe picks up the spoke's front motion of the $m = 1$ mode as it rotates in the device's cross section. Specifically, two cases are shown: (a) the Argon discharge simulated with only ionizing collisions, and (b) the Argon discharge simulated with ionizing and non-ionizing electron neutral collisions, i.e., elastic and excitation collisions. Figure 6 (top) shows a smoothened version of the ion density

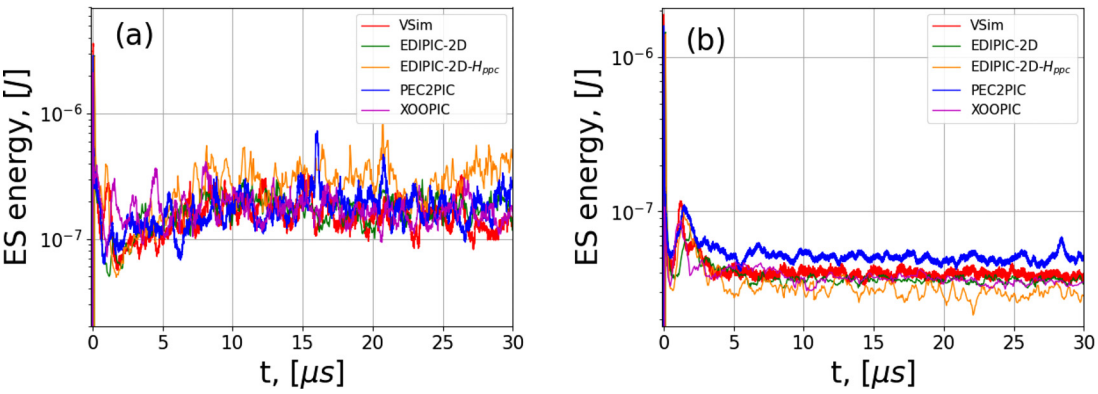

FIG. 3. Evolution of electrostatic energy with time; (a) case with only ionization collision, (b) case with ionization plus non-ionizing electron-neutral collisions. The data with a H_{ppc} label is from the simulations with a larger number of computational particles per cell (ppc), which is around 85 for case (a), and 127 for case (b).

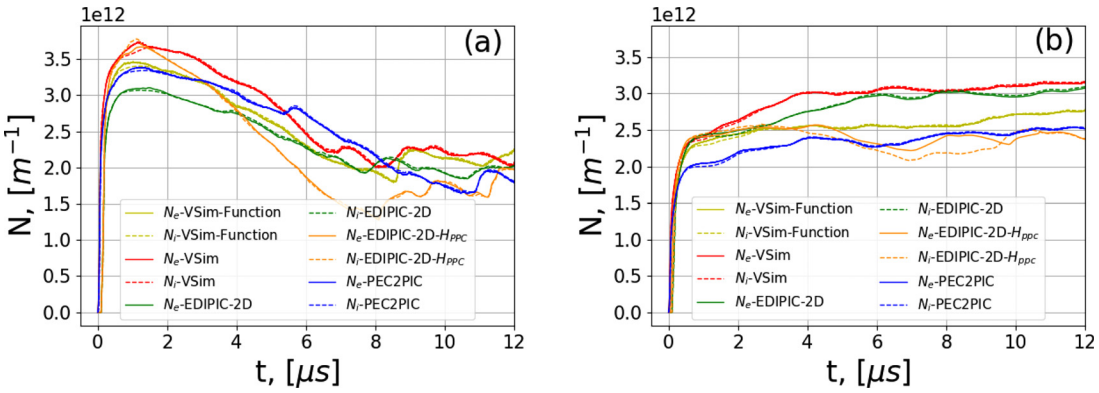

FIG. 4. The effect of different implementations of the scattering cross sections: (a) Argon discharge with only ionization only; (b) Argon discharge with ionization plus non-ionizing electron neutral collisions. The yellow lines show the result from VSim, using the same fit function as PEC2PIC. The data with a H_{ppc} label is from the simulations with a larger number of computational particles per cell (ppc), which is around 85 for case (a), and 127 for case (b).

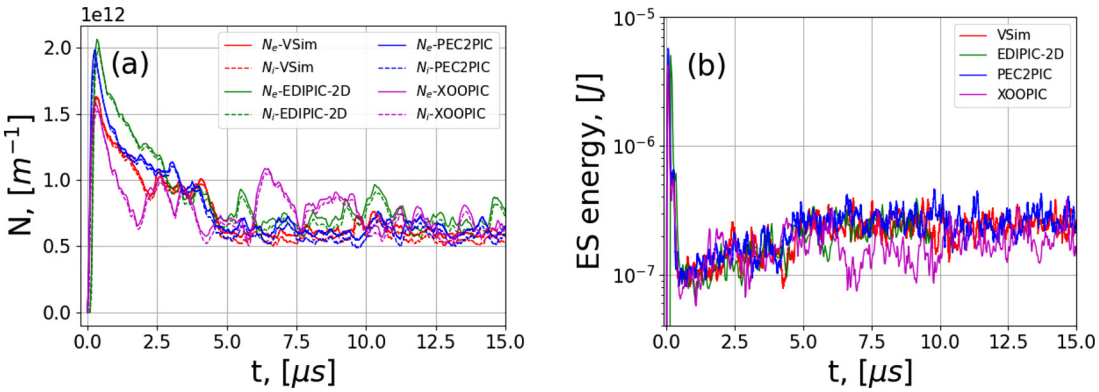

FIG. 5. Temporal evolution of (a) total particles inventory, (b) electrostatic energy of Hydrogen gas for simulation with ionization plus non-ionizing electron neutrals collision.

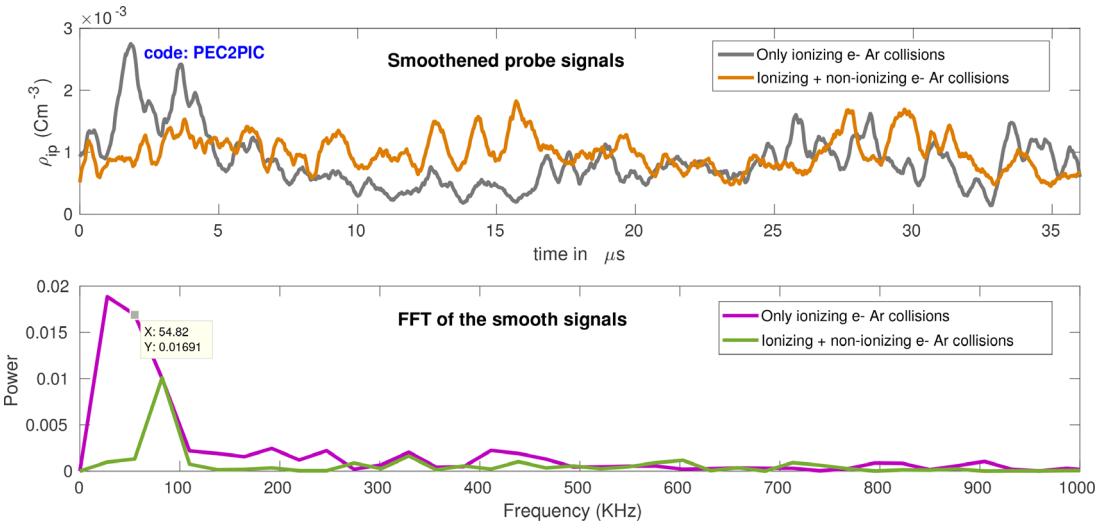

FIG. 6. The probe measurements results for the ion charge density, ρ_{ip}, and power spectrum showing the effects of collisions on the spoke frequency.

fluctuations at the probe for the two cases, while Fig. 6 (bottom) contains corresponding FFTs in time measuring the rotation frequencies. The smoothing is done with a moving average window with 0.4 ms time step. The probe signal's data points 5×10^{-11} s apart. We get a rotation frequency of about 55 kHz for PEC2PIC and 63 kHz for EDIPIC-2D for the case with only ionization and about 82 and 77 kHz correspondingly for the case with ionization plus non-ionizing collisions. The results show that the elastic electron scattering increases the rotation frequency of the spoke. Furthermore, the case with only ionization has a wider frequency peak compared to the case with ionization plus non-ionizing electron-neutral collisions.

The role of different types of collisions on the spoke frequency was also studied in EDIPIC-2D simulations. In Fig. 7, we show the temporal–spatial evolution of the ion density by visualizing the spoke rotation in EDIPIC-2D data. Here, a circular ring is considered at a quarter of the box size (half of a radius) with a width of 10 cells. The ring is split into 800 sectors so that the extent of one sector is roughly twice the cell size. The data are averaged over each sector area, and the information from all sectors is plotted as an angular dependence. One can clearly see the propagating density fronts corresponding to the rotating spoke structure. The front angle in the $\theta - t$ plane is used to measure the rotation frequency. There is good agreement between the spoke frequency measured from PEC2PIC simulations using local density probe data (Fig. 6) and from EDIPIC-2D simulations using temporal–spatial plots of the spoke fronts (Fig. 7). The diffused nature of the rotation frequency peak for the case with the ionization only (in the absence of all other electron-neutral collisions) is evident in both Figs. 7(a) and 6 (bottom). We have studied the convergence of the base case results by performing the additional EDIPIC-2D simulations with the higher average ppc numbers: 85 for the case with only ionizing collisions, and 127 for ionizing and electron-neutral non-ionizing collisions. The comparison shows that in the simulations with the higher ppc values, the quantitative characteristics do not change drastically: the difference in the averaged parameters is at most 15% reaching this maximum in the center of the domain. The rotation frequency for the $m = 1$ mode stays approximately the same since it is determined by plasma parameters in the bulk of the plasma, roughly at two-thirds of the radius, where the differences (in plasma parameters) are lower than 5%. We believe that such low sensitivity is due to the global nature of the $m = 1$ mode determined by plasma parameters in the central part of the discharge where the ppc number is significantly larger compared to the average value.

IV. AZIMUTHAL STRUCTURES AND SPECTRA

Here, we discuss the main characteristics of the $m = 1$ spoke and higher order $m > 1$ modes observed in the simulations and provide some interpretations regarding their nature. The simulations reported in this section have been performed in the square box $6 \times 6\,\text{cm}^2$ with the magnetic field of $B = 200$ G, particle weight is 3.1×10^5 (resulting in the ppc = 117), and the other parameters are the same as in Table I. Starting from this section, all presented results are acquired only for EDIPIC-2D. The simulation time is 200 ms, which takes about a month and a half on 400 hundred Central Processing Unit (CPU) cores from the Beluga server (Digital Research Alliance of Canada) for high ppc cases, and on 100 CPU hundred cores from the Niagara server (Digital Research Alliance of Canada) for low ppc cases. This results in eight full rotations if we start to count after the steady state has been reached (from 30 ms). No scaling technics have been used.

A. The $m = 1$ (spoke) mode

Formation in the nonlinearly saturated state of a large-scale rotating structure (spoke) is one of the most prominent features observed in our simulations. In the context of the Penning discharge geometry, similar structures were observed in experiments[1,2,11] and earlier simulations.[12,13]

It is instructive to discuss the ion rotation in the equilibrium in the absence of azimuthal perturbations. The ions are confined by the inward radial electric field. The ion rotation velocity in the equilibrium can be estimated from the radial momentum balance in the form

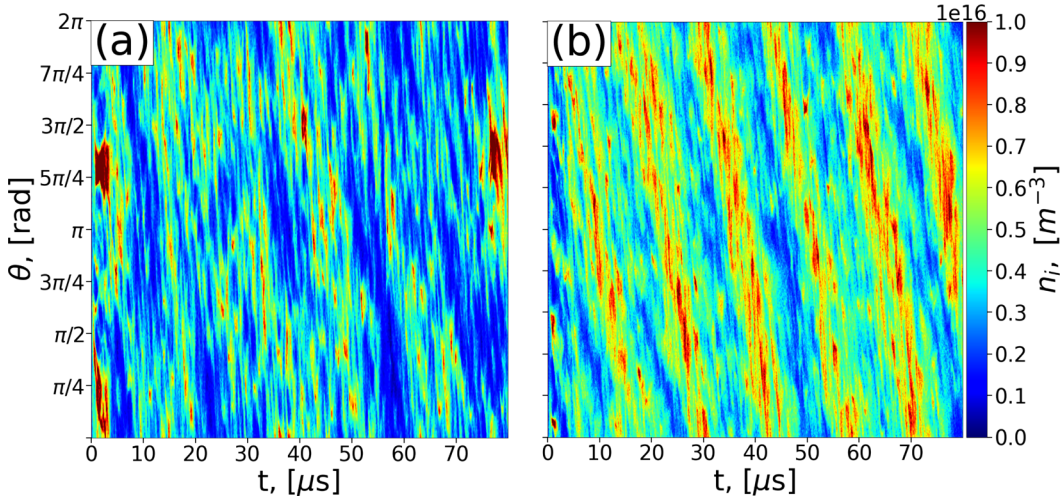

FIG. 7. Angular rotation of the ion density fronts: (a) the case when only ionizing collisions are included; (b) full electron neutral collisions and ionization are included. The spoke is dispersed and less evident when only ionization is included, consistent with the result of the probe measurements in Fig. 6.

$$-\frac{V_{\theta_i}^2}{r} = \frac{e}{m_i}[E_r + V_{\theta_i}B] - \frac{1}{m_i n}\nabla(T_i n_i). \quad (1)$$

The roots of Eq. (1) for $V_{\theta i}$ correspond to two branches of Brillouin rotation modes exploited in $E \times B$ filters for mass separation.[14] The Brillouin limit corresponds to the case of large $E_r > r\omega_{ci}B/4$ (in neglect of the pressure gradient) when the equilibrium is lost. In our case, the radial electric field is negative, ions are well confined, and the effect of the magnetic field on ions is small so that one has from Eq. (1) the following estimate for the frequency of the stationary ion rotation:

$$\omega_i \simeq \sqrt{\frac{-eE_r}{m_i r}}, \quad (2)$$

where $\omega_i = V_{\theta_i}/r$. Formally, for our parameters, the ion pressure gradient can be important; however, the effects of pressure gradient in its fluid form in Eq. (1) is not valid in the limit of large ion orbits so the kinetic theory has to be used. In our case, radial ion excursions are large and comparable to the device radius. As a result, the effects of the radial variations of density are largely smeared out for ions. In collisionless case, as for ions in our case, the distribution function is a function of the motion integral, e.g., $X = x + v_y/\omega_{ci} = const$, where x is a radial coordinate and X is a conserved quantity. Thus, the dependence on the radial coordinate x enters via X. Basically, it is impossible to have the radial gradient length scale much smaller than the Larmor radius.

As we will discuss in more detail below, the frequency from Eq. (2) well describes the $m = 1$ spoke rotation.

Figure 8 shows the $m = 1$ rotating structure in the evolution of the ion density, potential, and ion current. The values of the density, potential, and current do not follow each other locally; however, there is a good global correlation between the ion flow and potential suggesting ions are trapped by the potential. In other words, ions are globally confined by the inward radial electric field that supports the ion azimuthal rotation from Eq. (2). The global nature of the $m = 1$ structure and ion confinement (even with the spoke presently) is evident in the ion current flow, which occurs as a result of the rotation and wobbling of the ion cloud formed by the ionization [Fig. 8(c)]. The spoke rotation frequency remains close to the stationary ion rotation frequency given by Eq. (2).

Further insights on the spoke mechanism are obtained from the analysis of the electron current, ion and electron energies, and

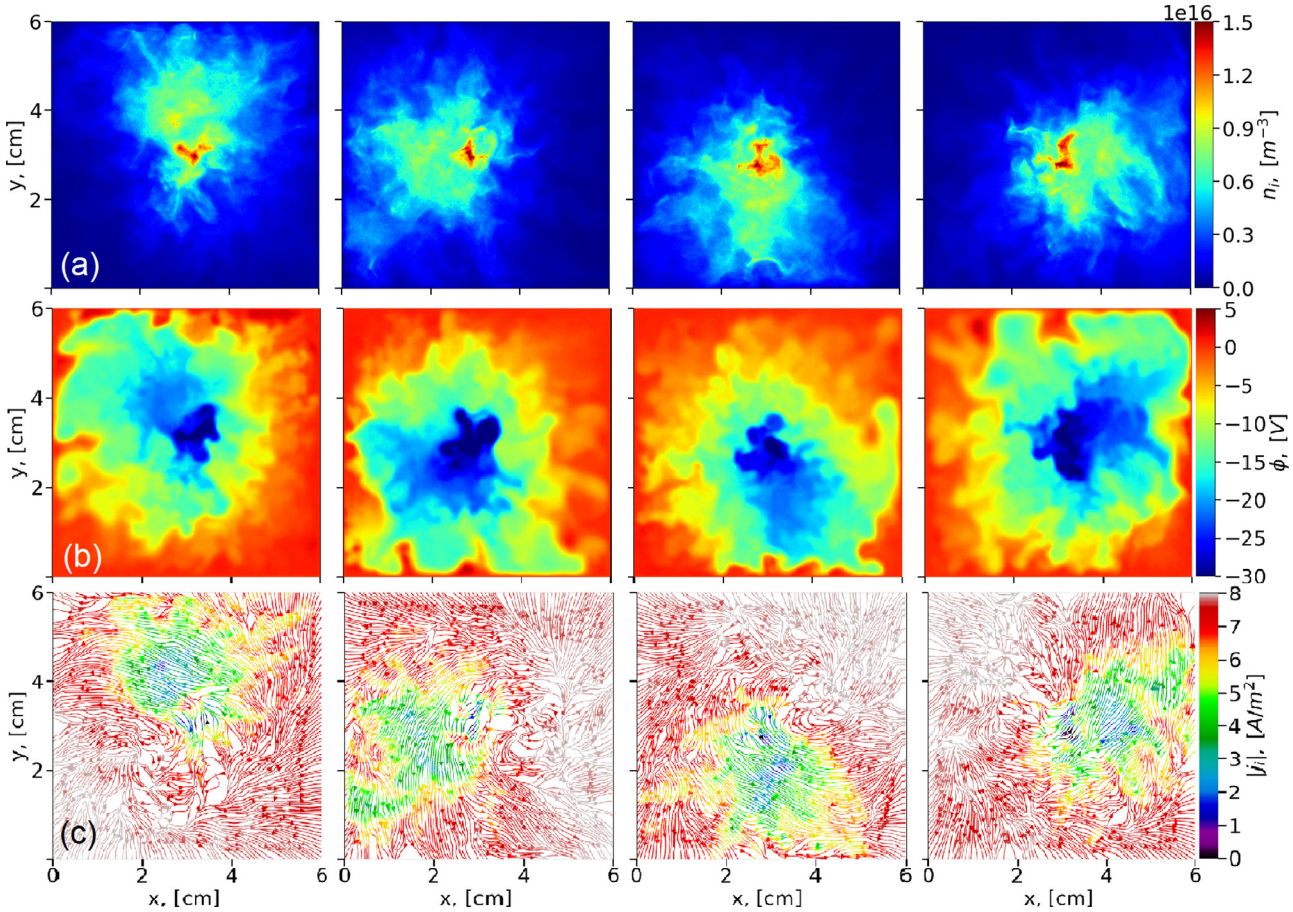

FIG. 8. Snapshots at different times, from left to right $t = 73, 79, 83$, and $88\ \mu s$, demonstrating spoke rotation: (a) the ion density; (b) the potential; (c) the ion current amplitude shown by the color and streamlines plotted on a uniform grid.

ionization rate in Fig. 10. One can see that the electron behavior is much more local compared to that of the ions. Electrons are locally heated in the regions of the strong electric field, at the edges of the potential structures where the gradients of the potential are large, as seen in Figs. 10(b) and 10(f). The regions of larger electron energy are well correlated with the regions where the ionization is most pronounced [Figs. 10(b), 10(d), and 10(f)]. The electron current concentrates inside narrow channels along the edges of the structures with large electron energy and enhanced ionization [Fig. 10(c)].

The ionization rates shown in Fig. 10(d) were directly obtained from the MCC collisions occurring in the code. Comparison with the ionization rates calculated for the Maxwellian distribution via the characteristic temperatures from Fig. 10(c) is an order of magnitude higher, thus suggesting that the tail of the electron distribution function is depleted compared to the Maxwellian. On the other hand, the actual average elastic collision frequency is close (within 8%) to the one calculated for the Maxwellian distribution. The 1D distributions are presented in Fig. 9.

It is interesting to note that the pattern of the ion energy distribution seems inverse to the distribution of the electron energy: the regions of the larger ion energy correlate with the regions of the lower electron energy Figs. 10(e) and 10(f). If they had the same magnitude, the sum of their energy would give almost uniform total energy. The ion energy is roughly equal to the energy of the ion stationary rotation, $T_i \propto m_i V_{i\theta}^2/2$, which means the ion energy is simply the kinetic energy of the oscillating ions trapped in the global rotating $m=1$ potential structure, while the electrons are heated by collisions and local electric field fluctuations as a result of the lower hybrid type instabilities.

B. Higher order modes, $m>1$

The dominant $m=1$ spoke structure is clearly distorted by the presence of higher m modes as seen from FFT power spectra in Fig. 11(b). Faster harmonics can also be seen inside the angular-time plots of the density [Fig. 11(a)].

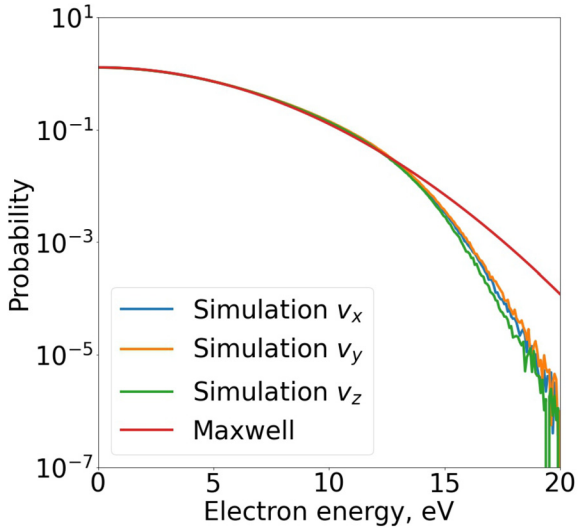

FIG. 9. Comparison of the measured 1D distributions (time average over two spoke rotations, taken in the bulk of plasma $R/4 < r < 3R/4$) with the Maxwell distribution built from perceived temperature (mean energy) received from the measured distributions.

The two-dimensional FFT is a direct method to study the spectra of the modes. Such an approach, however, is difficult to apply here because it demands a much longer simulation time with many rotation periods. We use the super-resolution signal processing tool—MUSIC (multiple signal classification) which is used also in Ref. 15. This method is not so strongly bound by the FFT frequency resolution limit and, most importantly, is less sensitive to noise compared to FFT.[16,17] Since we have a decent resolution in the angular direction, we transform each time slice in this direction with FFT, then we apply the MUSIC algorithm for each layer of k_θ to transform the time series to the frequency space. The output of this method is an array of frequencies and the main drawback is that the relative signal strength is not reflecting the true signal strength. Figure 12 displays the comparison between two approaches: the lower modes from both methods are in reasonable agreement, while the higher modes are seen only from the MUSIC algorithm.

We interpret the observed small-scale fluctuations as a result of gradient-drift instabilities that occur due to the radial electric field, density gradient, and collisions. The general linear dispersion relation for such modes in partially magnetized plasma has been proposed in Ref. 3. Taking into account the electron inertia, gyro-viscosity, and collisions, one has

$$k_\perp^2\lambda_D^2 + \frac{\omega_* + k_\perp^2\rho_e^2(\omega-\omega_0+i\nu_{en})}{\omega-\omega_0+k_\perp^2\rho_e^2(\omega-\omega_0+i\nu_{en})} - \frac{k_\perp^2 c_s^2}{\omega^2} = 0. \quad (3)$$

Here, ω_* is the diamagnetic drift frequency, $\omega_* = k_\theta v_* = T_e k_\theta / eB_0 L_n$, L_n is the gradient length given by $L_n^{-1} = -n_0'/n_0$, $\omega_0 = k_\theta v_E = -k_\theta E_{0r}/B_0$ is drift frequency, k_θ is angular wave vector in the azimuthal (θ) direction, k_r is the radial wave vector, $k_\perp^2 = k_\theta^2 + k_r^2$, ρ_e is the electron Larmor radius, c_s is the ion sound speed, E_{0r} is the radial electric field, and ν_{en} is the electron-neutral collision frequency.

The dispersion [Eq. (3)] also includes the finite Debye length effects, given by the term $k_\perp^2\lambda_D^2$, due to charge separation (non-quasineutrality). In the long-wavelength limit, $k_\theta\rho_e \ll 1$, one recovers from Eq. (3) collisionless Simon–Hoh instability[18] which occurs for $\mathbf{E}\cdot\nabla n_0 > 0$. For shorter wavelengths, the electron inertia results in the lower-hybrid mode that can be destabilized[3] by density gradients, $\mathbf{E}\times\mathbf{B}$ drift, and collisions. For larger $k_\theta\rho_e \geq 1$, the electron response becomes Boltzmann like and one has the ion sound type mode propagating perpendicular to the magnetic field

$$\omega^2 = k_\perp^2 c_s^2/(1+k_\perp^2\lambda_D^2). \quad (4)$$

It is important to note that in the limit of large collision frequency, $\nu_{en}k_\theta\rho_e \gg (\omega_0, \omega_*)$, the electron response [the second term in Eq. (3)], is also Boltzmann like and the mode again reduces to the ion sound. In the limit of large $k_\perp^2\lambda_D^2 > 1$, the electron density perturbations become small and one recovers the short wavelength ion sound mode: $\omega \to \omega_{pi}$, for $k_\perp^2\lambda_D^2 > 1$, where $\omega_{pi} = \sqrt{4\pi e^2 n_0/m_i}$.

In the collisionless limit, neglecting electron inertia, one recovers from Eq. (3) collisionless Simon–Hoh instability[3,11]

$$\omega = \frac{k_\perp^2 c_s^2}{2\omega_*} + \sqrt{\frac{k_\perp^4 c_s^4}{4\omega_*^2} - \frac{k_\perp^2 c_s^2}{\omega_*}\omega_0}. \quad (5)$$

For our parameters, the first term is small and the instability is almost aperiodic with the growth rate

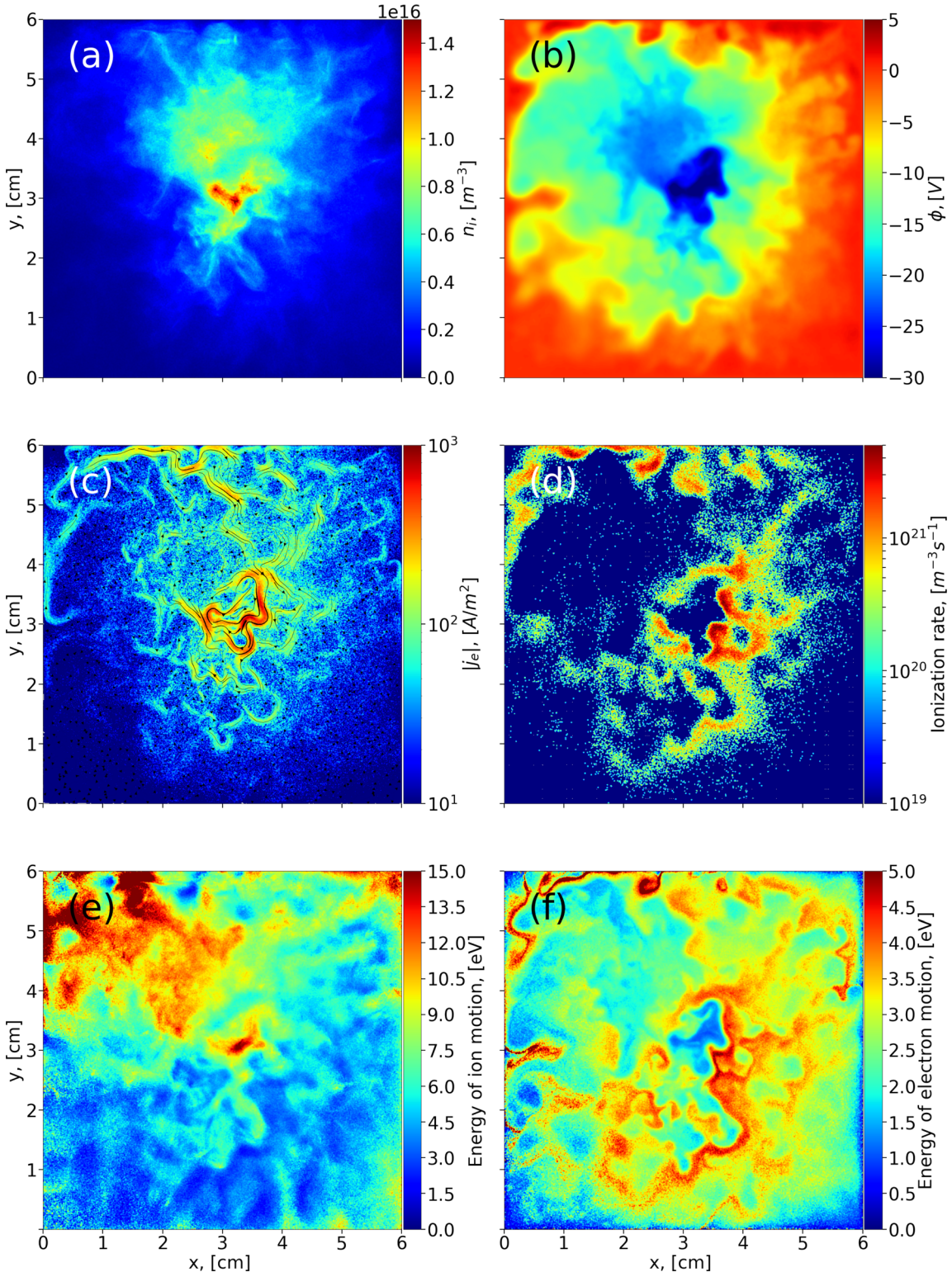

FIG. 10. Characteristic behavior of plasma parameters in the spoke regime at 73 μs: (a) ion concentration; (b) potential; (c) magnitude of the electron current density with streamlines (plotted on a regular grid); (d) ionization rate; total (e) ion and (f) electron energy.

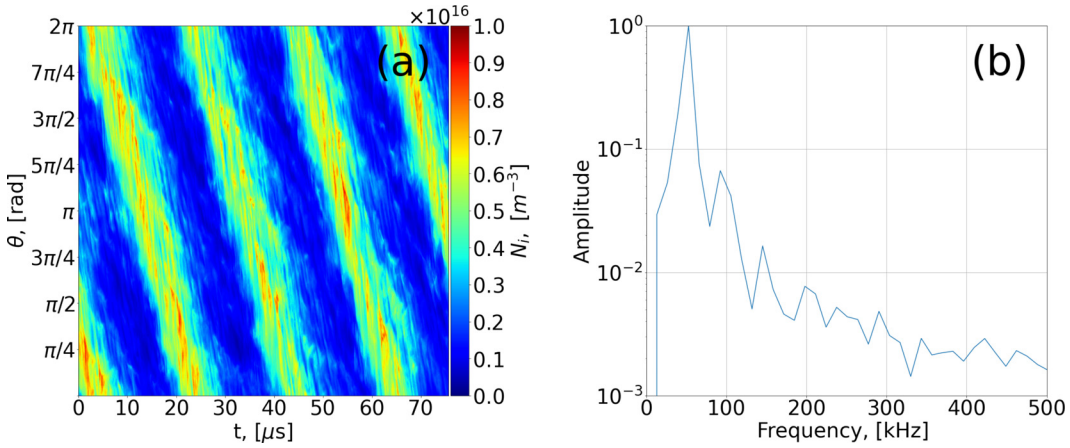

FIG. 11. Coexisting large- and small-scales modes. (a) Ion density evolution in the $\theta - t$ plane. The angle of the wavefronts corresponds to the angular frequency. One can see the faster, $m > 1$, modes inside the main $m = 1$ spoke structure. (b) The modes' power spectrum with a range of nonlinear harmonics.

$$\gamma = \sqrt{\frac{k_\perp^2 c_s^2}{\omega_*}\omega_0} = k\sqrt{\frac{eE_r L_n}{m_i}}. \tag{6}$$

This expression roughly corresponds to the spoke rotation frequency observed in simulations in Ref. 12. For $k \simeq 1/r$ and $L_n \simeq r$, the expression in Eq. (6) gives the same estimate as Eq. (2) for the equilibrium ion rotation. From Figs. 8(b) and 8(c), one can observe that the ion rotation has a character of the coherent wobbling of charged cloud [Fig. 8(b)], together with the ion beam [Fig. 8(c)]. Since the plasma density and electric field profiles are unstable with respect to the collisionless Simon–Hoh instability, one can conclude that the wobbling occurs as a result of this instability, while roughly maintaining the equilibrium rotation. The coincidence of the ion rotation velocity and the growth rate of the $m = 1$ mode also means that the same terms balance each other both in the equilibrium and in the perturbed dynamics. Namely, in the equilibrium, the ion inertia (centrifugal force) in the ion rotation is balanced by the electric field, while, in the perturbed state, the ion inertia, controlled by the electric field, determines the ion density. The electron density follows the electrostatic potential, and thus, via the quasineutrality, the ion inertia is balanced by the electric field, as in the equilibrium.

Equations (3) and (5) do not include ion equilibrium rotation. When the ion flow V_{θ_i} in the equilibrium is included, the frequency in the ion response part has to be modified by the Doppler shift $\omega \to \omega - k_\theta V_{\theta_i}$. Such modifications of Simon–Hoh instability were considered in Refs. 11 and 19.

For our conditions, the electron-neutral collision frequency is much larger than the spoke rotation frequency. Therefore, to compare the results of numerical solution with the $\omega - k_\theta$ spectra of the $t - \theta$: E_θ field obtained in simulations during the saturated state, we use full Eq. (3) with collisions and take into account the modification of the ion response due to the ion rotation, i.e., use $\omega \to \omega - k_\theta V_{\theta_i}$. Such comparison is shown in Fig. 13 for our typical plasma parameters listed in Table II, which are the result of azimuthal averaging at a half

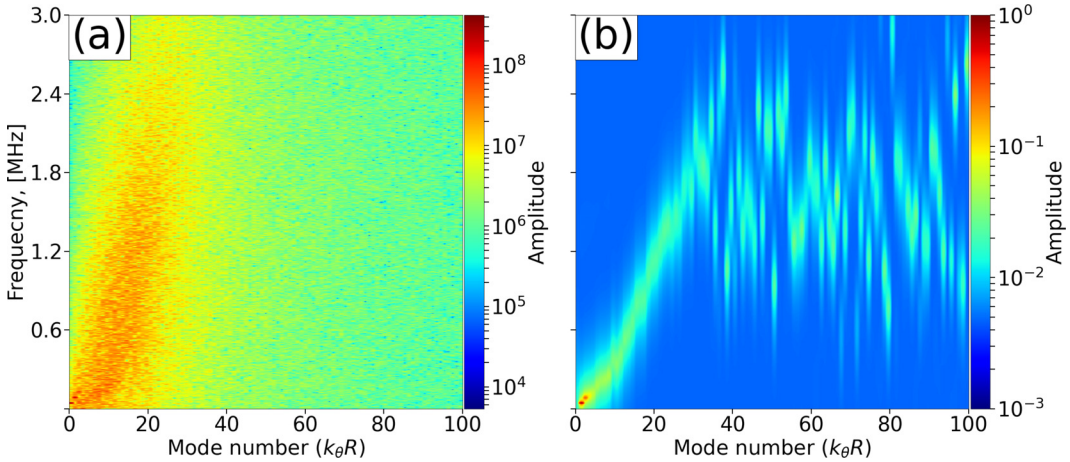

FIG. 12. Comparison between (a) 2D FFT and (b) 1D Fourier in angle variable and MUSIC in time. The MUSIC spectra below $m = 30$ are consistent with the 2D FFT noisy signal. The higher m modes above $m = 30$ are only seen with MUSIC.

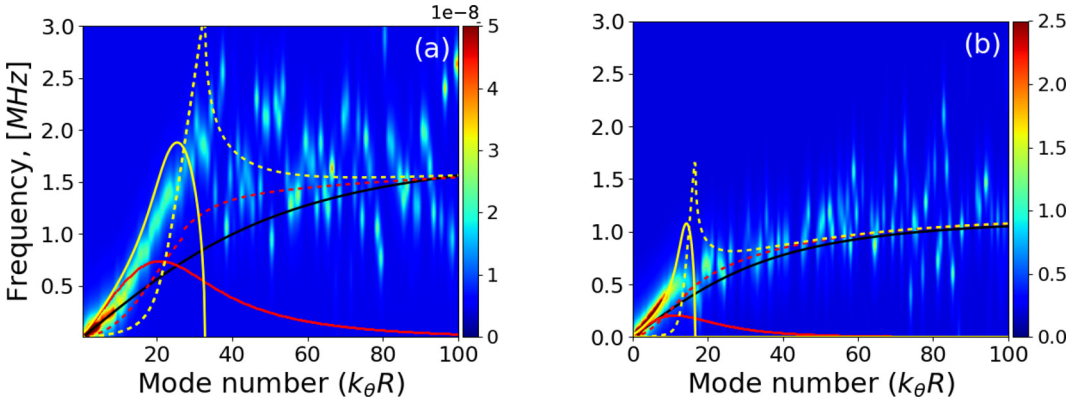

FIG. 13. The 1D FFT+MUSIC transform of the space–time data of E_θ from simulations. Theoretical values of the real and imaginary frequency from Eq. (3) are shown as dashed and solid lines, respectively, for collisionless $\nu_{en} = 0$ (gold), and collisional $\nu_{en} = 1.2 \times 10^8$ s^{-1} (red) cases for parameters in Table II. The theoretical results include Doppler shift due to equilibrium ion rotation. The black line shows the ion sound wave dispersion from Eq. (4): (a) $B = 200$ G and (b) $B = 50$ G.

a radius distance for two values of the magnetic field: $B = 50$ G and $B = 200$ G. With collisions, Eq. (3) predicts the instability with a real part of the frequency similar to the ion-sound mode. In the formal limit $\nu_{en} \to \infty$, one recovers from Eq. (3) the ion-sound mode, as shown in Eq. (4). This is also shown by the black line in Fig. 13. One can see that the real part of the frequency in the collisional case starts to resemble the ion sound mode (shown by a black line) and the effect is stronger for the lower magnetic field, as in Fig. 13(b). Nevertheless, these modes have to be classified as the gradient-drift modes because the instability is caused by density gradient and collisions. The dissipation results in the positive feedback phase shift between the density and potential perturbations leading to the mode growth.[3] The growth rate in the collisional case is shown Fig. 13(a) by the solid red line.

Only qualitative agreement can be expected (at best) between the results of the local linear theory with nonlinear spectra of oscillations in the saturated state. Nevertheless, general trends are in agreement with predictions based on the gradient-drift instabilities from Eq. (3). The lower m modes are less affected by finite collisionality though it remains important, especially for the lower magnetic field as Fig. 13(b).

TABLE II. Local values of plasma parameters and spoke frequency f for different values of the magnetic field at $r = R/2$. The data were averaged in steady state over 2D snapshots (the time step between snapshots is 0.05 ms).

Quantity name \ Magnetic field, G	50	75	100	150	200	250	300
$-E_r$, V/cm	2.43	3.19	3.75	4.87	5.86	6.79	6.87
$-L_n$, cm	1.55	1.44	1.43	1.55	1.62	1.58	1.67
n_p, 10^{15} m^{-3}	1.23	1.74	1.95	2.37	2.64	2.95	3.36
T_e eV	2.68	3.14	3.09	3.02	2.99	2.98	3.37
ν_{en}, 10^8 s^{-1}	1.01	1.32	1.30	1.27	1.26	1.25	1.70
f, kHz	31.7	36.9	37.1	41.4	46.7	51.8	53.1
f_{cs}, kHz (c_s/r)	84.5	91.4	90.6	89.7	89.2	89.1	94.7

Increasing collision frequency shifts the real part of the frequency to a higher value while decreasing the growth rate. This provides the justification for the result in Fig. 6 that shows that including non-ionizing electron neutral interaction increases the rotation frequency of the spoke and makes the peak wider.

The equilibrium ion rotation also affects the low m modes as shown in Fig. 14. The ion rotation increases the real part of the frequency so that the growth rate and real part become very close to each other for $m = 1$ mode, see Figs. 14(c) and 14(d).

The dynamics of the low m modes are affected by the inverse cascade predicted for these systems earlier.[3,20,21] Merging of higher m modes into the dominant $m = 1$ is evident in Fig. 15(b). The initial $m = 4$ mode and its $m = 8$ harmonics correspond to the initial periodicity of the square geometry of the simulation box. With time, these modes are reduced, and $m = 1$ and $m = 2$ emerge, which grow in amplitude until they reach a steady state with a dominant $m = 1$ mode. The weak high m modes with $m > 10$ also visibly reduce with time in Fig. 13. Nevertheless, some activity of higher m modes remains present as shown in Figs. 11(a) and 11(b).

V. PARAMETRIC STUDY OF THE $m = 1$ SPOKE CHARACTERISTICS AS A FUNCTION OF THE MAGNETIC FIELD, BOX SIZE, AND THE ION SPECIES

As it was discussed in Sec. IV, while the spoke mode originates from the gradient-drift instability the steady state spoke rotation frequency is well approximated by the Eq. (2) for the equilibrium ion rotation. We will use it to compare with the measured $m = 1$ frequency for different plasma parameters. We also show the profiles of plasma density, potential, and temperature for different cases. The radial electric field (E_r), the gradient length scale ($L_n^{-1} = n_p'/n_p$), plasma density (n_p), electron temperature (T_e), and electron-neutral collision frequency (ν_{en}) are acquired from the ring at a half of a radius. The electron temperature here is simply a measure of the averaged energy and is defined as follows: $T_e = (T_x + T_y)/2$, where $T_{x,y} = m(\langle v_{x,y}^2 \rangle - \langle v_{x,y} \rangle^2)$ are electron temperatures in the directions of x and y. As it was mentioned above, our convergence studies had determined that the spoke is resilient to noise due to the low ppc number. Comparison of the simulations with ppc = 117 and

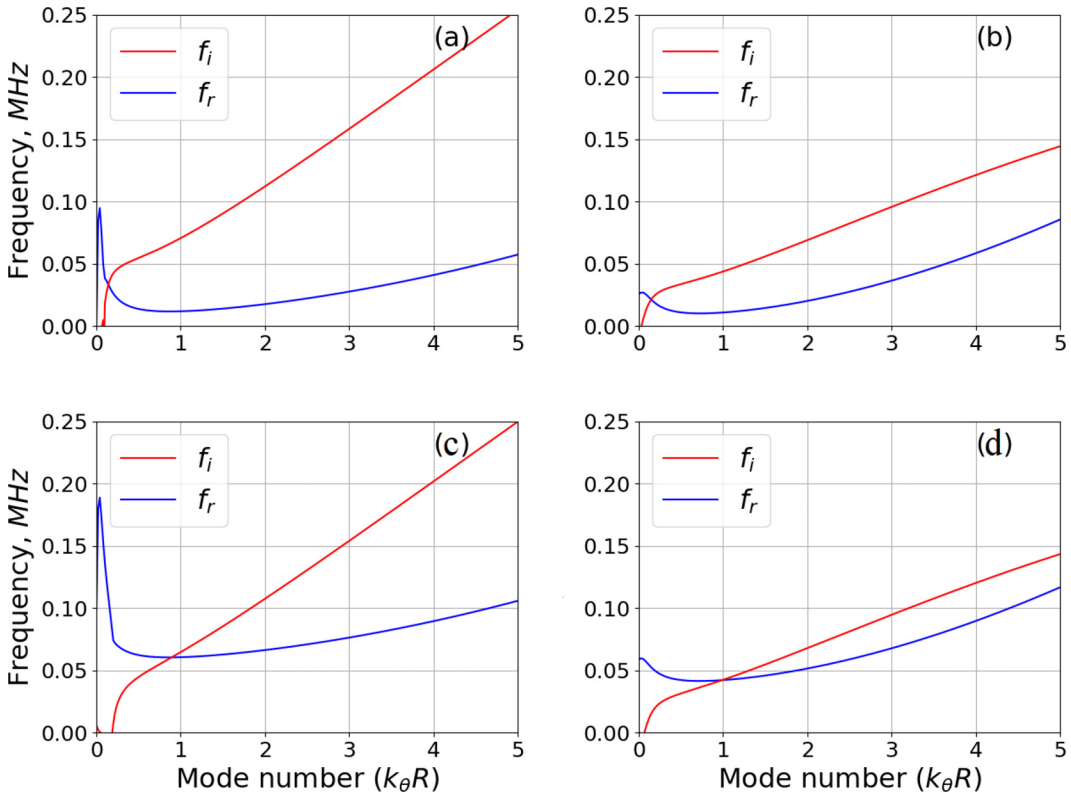

FIG. 14. The low m modes linear growth rate (red) and frequency (blue) with collisions and without the equilibrium ion rotation [Eq. (3) without Doppler shift: (a) $B = 200$ G; (b) $B = 50$ G, and with collisions and the Doppler shift equilibrium due to ion rotation from Eq. (2)] [with the replacement $\omega \to \omega - k_\theta V_{\theta i}$ in Eq. (3)] (c) $B = 200$ G; (d) $B = 50$ G.

ppc = 11 for the 6×6 cm^2 case shows qualitatively similar behavior while quantitatively the difference in averaged parameters is at most of the order of 5%–6%. As it was noted above, this is explained by the fact that the actual ppc in the central part of the simulation domain is higher compared to the averaged value. In this section, the scalings for the averaged parameters and $m = 1$ frequency are shown for the low resolution cases with the averaged ppc of the order of 10 (particle weight is 3×10^6).

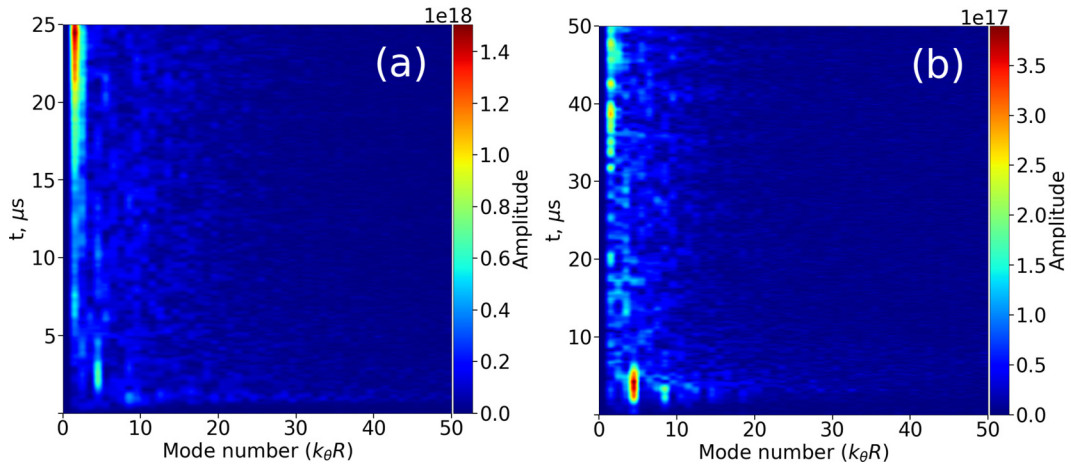

FIG. 15. The azimuthal electric field E_θ at $r = R/2$ is transformed by 1D FFT method in the angle direction, at each time step for (a) $B = 200$ G and (b) $B = 50$ G. For both cases, the inverse energy cascade can be observed as time progresses.

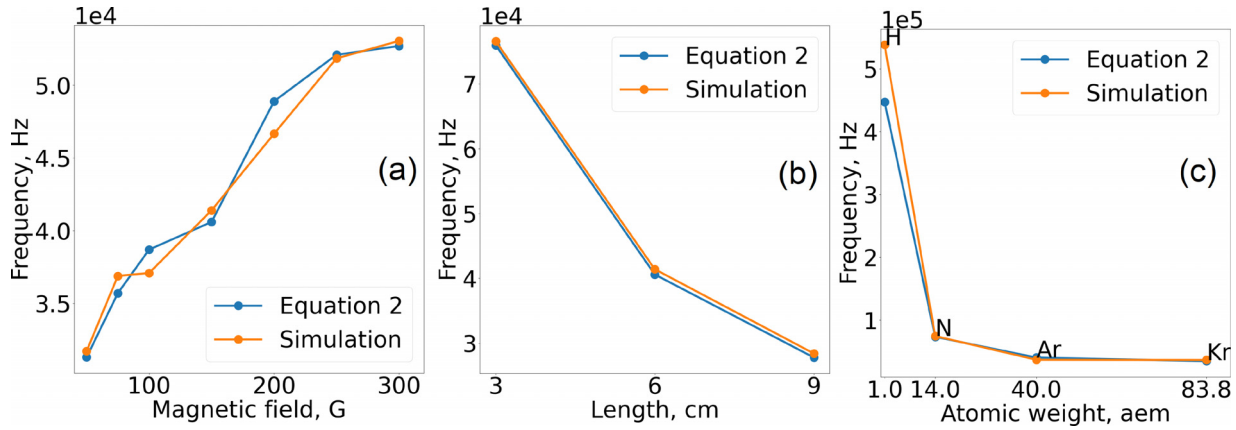

FIG. 16. The spoke rotation frequency as a function of (a) magnetic field; (b) size, and (c) atomic element.

A. Effects of the magnetic field

Variation of the spoke frequency with the magnetic field obtained in simulations and comparison with the theoretical value from Eq. (2) is shown in Fig. 16(a). Variation of plasma parameters profiles with the magnetic field is shown in Fig. 17 and typical local values are summarized in Table II. The magnetic field does not explicitly enter the Eq. (2). Its effect, however, is manifested via the electric field dependence which is seen in Figs. 17(c) and 17(d) and Table II. Increasing the axial magnetic field improves plasma confinement; therefore, increasing the depth of the potential well and the local radial electric field at $r = R/2$. Global confinement of plasma density is also improving with the magnetic field [see Fig. 17(a)], but the local value of the gradient length scale does not change much with the magnetic field and remains around 1.5 cm, which corresponds to the effective radius for this case with 3×3 cm simulation box. As it is shown in Fig. 16(a), the spoke frequency roughly follows the $\sqrt{B}$ scaling. This scaling was proposed in Ref. 12 based on the expression for the growth rate of the Simon–Hoh instability given by Eq. (6). As it was explained in Sec. IV, those expression becomes similar to Eq. (2) for $m = 1$ mode and constant $L_n \simeq r$ parameter as in the current simulations.

B. The spoke frequency scaling with the size of the simulation box

The box size scaling shows clear dependence of the $m = 1$ mode frequency as R^{-1}, see Fig. 16(b) and Table III (for summarized typical values). The radial dependence of plasma parameters are demonstrated in Fig. 18.

C. Effects of the ion species

The radial profiles of plasma parameters for different elements are shown in Fig. 19 and summarized in Table IV for other parameters are from Table I. The atomic element scaling in Fig. 16(c) is in good agreement with $\sim M^{-1}$ dependence, thus suggesting that the electric field varies with the atomic element roughly as $\sim 1/\sqrt{M}$. In simulations, the exact ionization energies for different elements were used; however, the importance of this factor is difficult to evaluate since the ionization energies for these elements are rather close. As it is shown in Figs. 10(d) and 10(f), there is a notable increase in the electron temperature and ionization rate at the edges of the $m = 1$ potential structure. This enhanced ionization, however, does not explain the rotation velocity, at least not within the standard concept of the Critical Ionization Velocity (CIV) phenomenon,[22] in which the velocity of the ionization front is limited by the CIV value $\sqrt{2eV_{ion}/M}$, where V_{ion} is the ionization potential. As shown in Table V, the spoke rotation velocity observed in simulations is much lower than the CIV value. We note that in all cases, the $m = 1$ spoke rotation is much slower than the $\mathbf{E} \times \mathbf{B}$ values.

VI. THE SMALL-SCALE SPIRAL ARMS STRUCTURES REGIME

In this section we investigate the transition to the regime in which small-scale spiral arms azimuthal structures occur, similar to those observed in Ref. 23. For our simulations, we use the box with size $6 \times 6\,\text{cm}^2$ with Argon and the magnetic field is 150 G, achieved ppc number is around 90, other parameters are the same as in Table I.

In our simulations, there are two mechanisms of the energy input to the discharge. One mechanism is the kinetic energy (in the axial z-direction) of injected electrons. With sufficient initial kinetic energy, such electrons may produce ionization directly. After scattering on neutrals, these electrons acquire a finite velocity in the x-y plane and start to move radially as a result of further collisions and fluctuating electric fields. For our base case parameters, the radial motion of injected electrons as well as electrons and ions produced by ionization typically establishes the radial electric field directed inward, e.g., see Fig. 17(c). Injected electrons diffusing radially outward create the inward electric current. In the stationary state, the value of this current is equal to the injection current which is fixed as an external parameter, while the radial electric field establishes self-consistently as a result of the power and particle balance. Co-directed electric field and current in radial direction represent the second mechanism of the energy input to the discharge. For the parameters of our base case, exhibiting the $m = 1$ spoke activity, the second mechanism is dominant, as the axial energy of the injected electrons is low, see Table V. For the base parameters, the axial kinetic energy of the injected electron is in fact below the ionization energy so they are unable to produce ionization directly. The electrons are heated as a result of small-scale instabilities of the

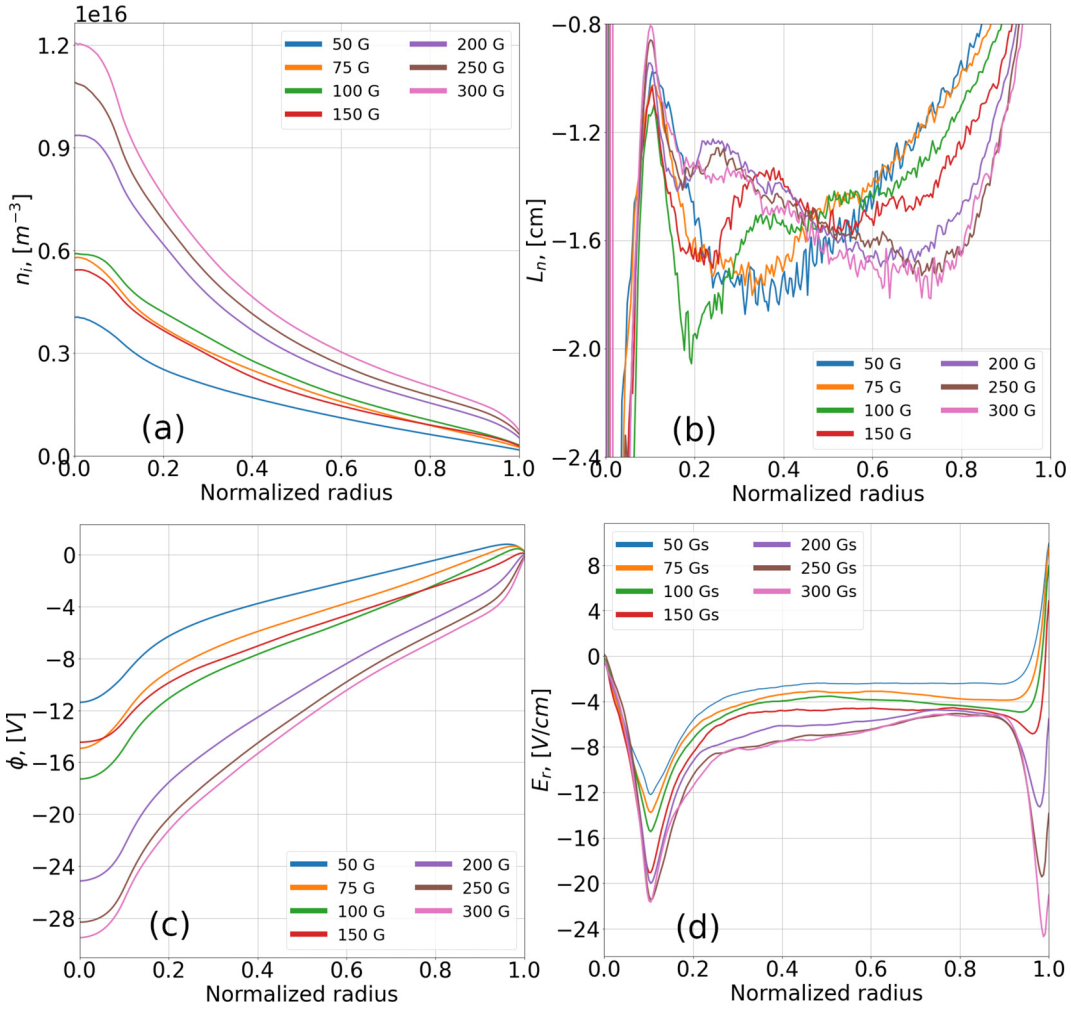

FIG. 17. Radial profiles of plasma parameters for different magnetic fields: (a) ion concentration; (b) gradient length scale; (c) potential; and (d) electric field.

lower-hybrid type. Releasing cold electrons inside of the injection region with the same current produces a very similar result.

We observe the disappearance of the $m = 1$ spoke activity when the power absorption mechanism and the total power delivered to the discharge reduce. To facilitate the comparison, we increase the axial beam energy to maintain roughly the same plasma density in the center. 5×10^{15} m^{-3}. More precisely, we perform a series of numerical experiments for different values of the injection kinetic energy, adjusting the injection current in each case to maintain the central plasma density near the target value. The values for the injection energy, beam current, beam power, and radial current power for these simulations are given in Tables VI and VII. As the energy delivered by the radial current decreases, the spoke activity is gradually reduced, the spoke becomes slower, and the system enters the regime with a smaller scale, $m > 1$ spiral arms structures, as in Fig. 20. The transition occurs around the injection energy of 20 eV. Change of the regime is continuous, e.g., even for the case of 30 eV one can see some spoke signatures around 13 kHz [Figs. 22(a) and 22(b)]. However, the power in the low frequency region corresponding to the spoke frequency is low compared to the spectral power for arms structures in the range of frequencies 400–800 kHz. Further increase in the energy of injected electrons leads to even more weakened spoke and less noisy high k modes (Fig. 23). The spoke frequency rotation is slowing down, and the number of arms and their frequency is increasing: injection with 50 eV produces 7 and 600–900 kHz, for the spoke and spiral modes, respectively.

Figure 20 present the snapshots of the characteristic behavior of plasma parameters in the small-scale regime exhibiting multiple spiral arms structures for the injection energy of 30 eV. The plasma density, potential, ion, and electron energy, and ion flow are all rather coherent and well correlated with the spiral structures. Ionization mostly occurs on the outskirts of the injection region as a ring due to the direct impact of the injected electrons.

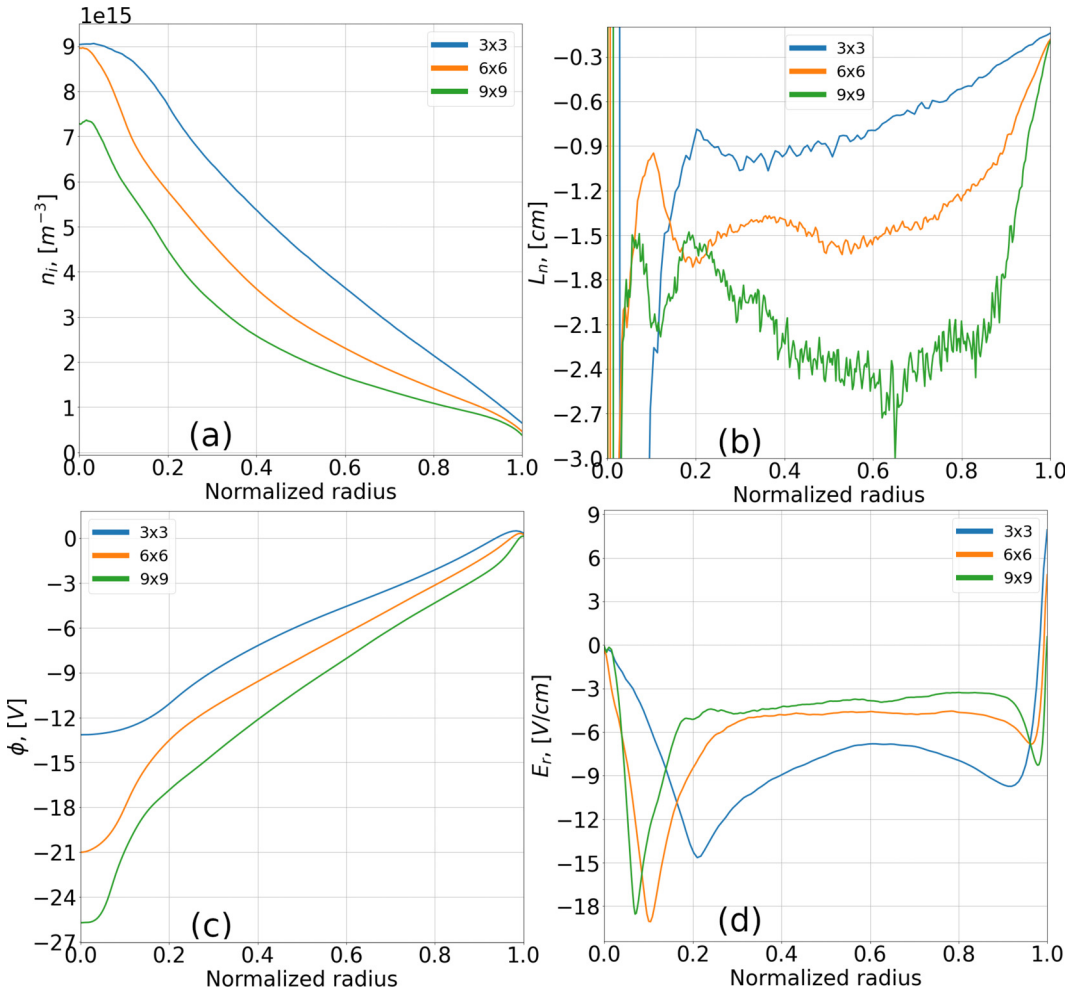

FIG. 18. Radial profiles of plasma parameters for different size of the simulation box: (a) ion concentration; (b) gradient scale length; (c) potential; and (d) electric field.

The important feature of small-scale regime is a significant reduction of the radial electric field so the potential flattens and may even become slightly positive in the center (Fig. 21). In this case, the remaining instability mechanism is the combination of the density gradient and collisions.[3]

The comparison of the fluctuations spectra observed in simulations with the theoretical dispersion from Eq. (3) is given in Fig. 23. In this regime, the real part of the frequency is very close to the ion sound mode with the growth rate defined by the density gradient and collisionality.

TABLE III. Local values of $E_r, L_n, n_p, T_e, \nu_{en}$.

Quantity name \ Size, cm^2	3×3	6×6	9×9
$-E_r$, V/cm	7.13	4.87	3.81
$-L_n$, cm	0.86	1.55	2.40
n_p, 10^{15}m^{-3}	4.06	2.37	1.86
T_e eV	3.27	3.02	2.7
ν_{en}, 10^8s^{-1}	1.41	1.27	1.12
f, kHz	76.6	41.4	28.4
f_{cs}, kHz	187	89.6	62.2

TABLE IV. Local values of $E_r, L_n, n_p, T_e, \nu_{en}$.

Quantity name \ Element	H	N	Ar	Kr
$-E_r$, V/cm	12.35	5.72	4.87	6.34
$-L_n$, cm	1.91	1.41	1.55	1.62
n_p, 10^{15}m^{-3}	0.95	2.55	2.37	1.33
T_e eV	3.08	2.96	3.02	1.63
ν_{en}, 10^8s^{-1}	0.83	9.90	1.27	2.93
f, kHz	538	74.8	41.4	36.7
f_{cs}, kHz	573	153	89.6	62.5

TABLE V. CIV and spoke rotation velocity.

Element	Mass, amu	V_{ion}, eV	CIV, 10^3 m/s	Spoke velocity, 10^3 m/s	$E \times B$ velocity, 10^3 m/s
Hydrogen	1	13.6	51	2.57	82.3
Nitrogen	14	14.5	14.1	0.36	38.1
Argon	40	15.75	8.7	0.2	32.4
Krypton	83.8	14	5.66	0.18	43.3

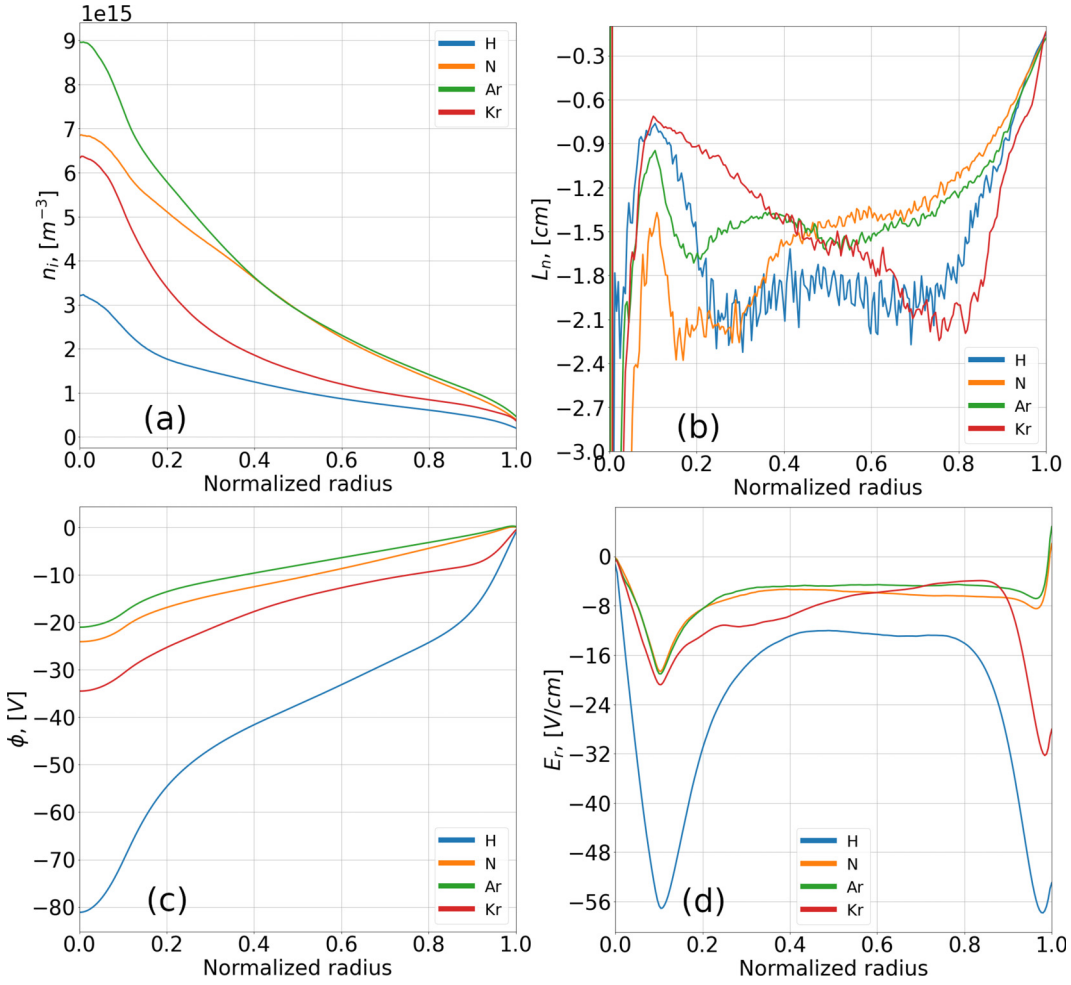

FIG. 19. Radial profiles of plasma parameters for different atomic elements: (a) ion concentration; (b) gradient scale length; (c) potential; and (d) electric field.

TABLE VI. Input power due to the axial electron beam and $\mathbf{J} \cdot \mathbf{E}$.

Quantity name \ Electron energy, eV	0	5	10	15	20	30	40	50
Axial beam power, $J\,s^{-1}m^{-1}$	0.00	0.28	0.49	0.48	0.22	0.214	0.213	0.212
$\int \mathbf{J} \cdot \mathbf{E} dxdy$, $J\,s^{-1}m^{-1}$	1.92	1.43	0.80	0.30	0.02	0.026	0.021	0.03
Axial beam current, $A\,m^{-1}$	0.04	0.06	0.056	0.03	0.01	0.007	0.005	0.004

TABLE VII. Characteristic local plasma parameters for small-scale regime at $r = R/2$, $B = 150$ G, for Argon.

Quantity name \ Electron energy, eV	0	5	10	15	20	30	40	50
$-E_r$, V/cm	1.41	0.99	0.74	0.33	0.31	0.09	0.04	0.02
$-L_n$, cm	2.71	2.81	2.49	2.64	2.37	2.24	2.33	2.39
n_p, $10^{15}\mathrm{m}^{-3}$	0.82	0.79	0.65	0.51	0.47	0.62	0.71	0.76
T_e eV	2.46	2.49	2.46	2.28	1.92	1.79	1.74	1.71
ν_{en}, $10^{8}\mathrm{s}^{-1}$	1.01	1.02	1.01	0.92	0.76	0.69	0.67	0.65

VII. TURBULENT TRANSPORT AND MOBILITY

In this section, we discuss and compare the magnitude of the radial current in the $m = 1$ spoke and small-scale modes regimes. The radial profiles of the electron and ion current are shown in Fig. 24. The spoke regime shows a much larger total current. We characterize the net radial transport as the effective mobility and diffusion by using the representation in the form

$$j_e(r) = \mu_{eff}(r)\left[en_eE_r(r) + \frac{\partial}{\partial r}[n_e(r)T_e(r)]\right]. \tag{7}$$

The radial mobility profiles for μ_{eff} and contributions of the radial electric field (mobility) and pressure gradient (diffusion) are shown in Figs. 25 and 26. The effective mobility for the spoke regimes is almost the order higher than classical values and for the spiral arms regimes, it is several times larger. The relative contributions of the mobility and diffusion are shown in Fig. 25. For the spoke regime, the mobility flux (due to the radial electric field) is dominant, whereas the diffusion (due to the radial pressure gradient) part is prevailing in the spiral arms regime in the bulk plasma ($r/R > 0.2$).

It is useful to consider the relative contributions of fluctuations and classical transport to the radial current. Neglecting inertia in the electron momentum equation and separating the stationary and fluctuation parts in the electric field and density, $\boldsymbol{E} = \boldsymbol{E_0} + \tilde{\boldsymbol{E}}$, $n = n_0 + \tilde{n}$, one obtains an equation for the radial electron current (derivation can be found in Appendix C):

$$j_e^r = \frac{\nu e^2 n_0}{(1+\nu^2/\omega_c^2)m_e\omega_c^2}\left(E_r + \frac{1}{en_0}\frac{\partial p}{\partial r}\right) + \frac{e^2\nu}{m_e\omega_c^2}\frac{\langle\tilde{E}_r\tilde{n}\rangle}{1+\nu^2/\omega_c^2} - \frac{e^2}{m_e\omega_c}\frac{\langle\tilde{n}\tilde{E}_\theta\rangle}{1+\nu^2/\omega_c^2}. \tag{8}$$

Two last terms in this equation describe the turbulent transport, while the first two are the classical (collisional) contributions. Averaging over time ($\Delta t = 5\times10^{-7}$ s) and space the radial electron current can be compared to the results from the simulations (Fig. 27). For the spoke case, the dominant contribution is due to the fluctuations, $\langle\tilde{n}\tilde{E}_\theta\rangle$ [Fig. 27(a)], whereas in the spiral arm case the contribution of the fluctuations is of the same order as from the magnetized collisional diffusion [Fig. 27(b)]. We note that for the spoke regime, the expected contributions of different terms agree well with the measured current, while for the spiral arms case there is some difference [Fig. 31(b)]. This difference is possibly due to the contributions of the inertial and stress tensor contributions which are not included in our calculations. The small-scale arms case may also require a higher resolution to achieve a better agreement.

VIII. SUMMARY AND DISCUSSION

In this paper, we have studied fluctuations in the cylindrical Penning discharge self-consistently supported by the ionization from the electron beam. The discharge saturation to the steady-state was investigated with four different PIC codes: EDIPIC-2D, PEC2PIC, Vsim, and XOOPIC. It was found that while all codes show qualitatively the same behavior, some quantitative differences in plasma density (up to the order of 20%) may occur due to the differences in how the particle collisions and relevant cross-sections are implemented.

Two different regimes of turbulent structures and transport were revealed in the simulations: the $m = 1$ spoke regime with the large level of anomalous transport and the regime with small-scale $m > 1$ spiral arm azimuthal structures. A characteristic feature of the spiral arm regime is the flat profile of the potential, while in the spoke regime there is a deep potential well confining ions radially. The spiral arm regime is much quieter and has turbulent transport which is only several times larger than the classical one due to collisions. One has to note that the transition between the two regimes is continuous and low m (spoke) modes and high m (spiral arm) modes co-exist. In the case of the spoke, most of the power (in the sense of the FFT power spectrum density) is contained within a few first low-frequency modes (spoke modes $10 - 100$ kHz). On the contrary, in the spiral arms regime, the low m modes are weak, and the power is concentrated within a wide range of high-frequency modes (spiral arms $0.4 - 1$ MHz).

One of the goals was the investigation of the nature of large-scale $m = 1$ spoke activity often observed in experiments.[1,2] The comparison of the fluctuations spectra in the spoke regime, obtained with MUSIC and FFT algorithms, shows reasonable agreement with the theoretical dispersion relation and demonstrates the existence of the inverse cascade of energy toward the large scale. We have performed parametric studies of the spoke frequency with the magnetic field, simulation box size, and ion species which, in general, are similar to those found in Ref. 12. It is demonstrated that the spoke frequency is mostly determined by the radial electric field and follows the equilibrium ion rotation frequency. The observed dependence on the magnetic field is due to the variation of the radial electric field E_r: for larger values of the magnetic field, plasma confinement is improved resulting in the increase of the E_r and the spoke rotation frequency according to Eq. (2). We have

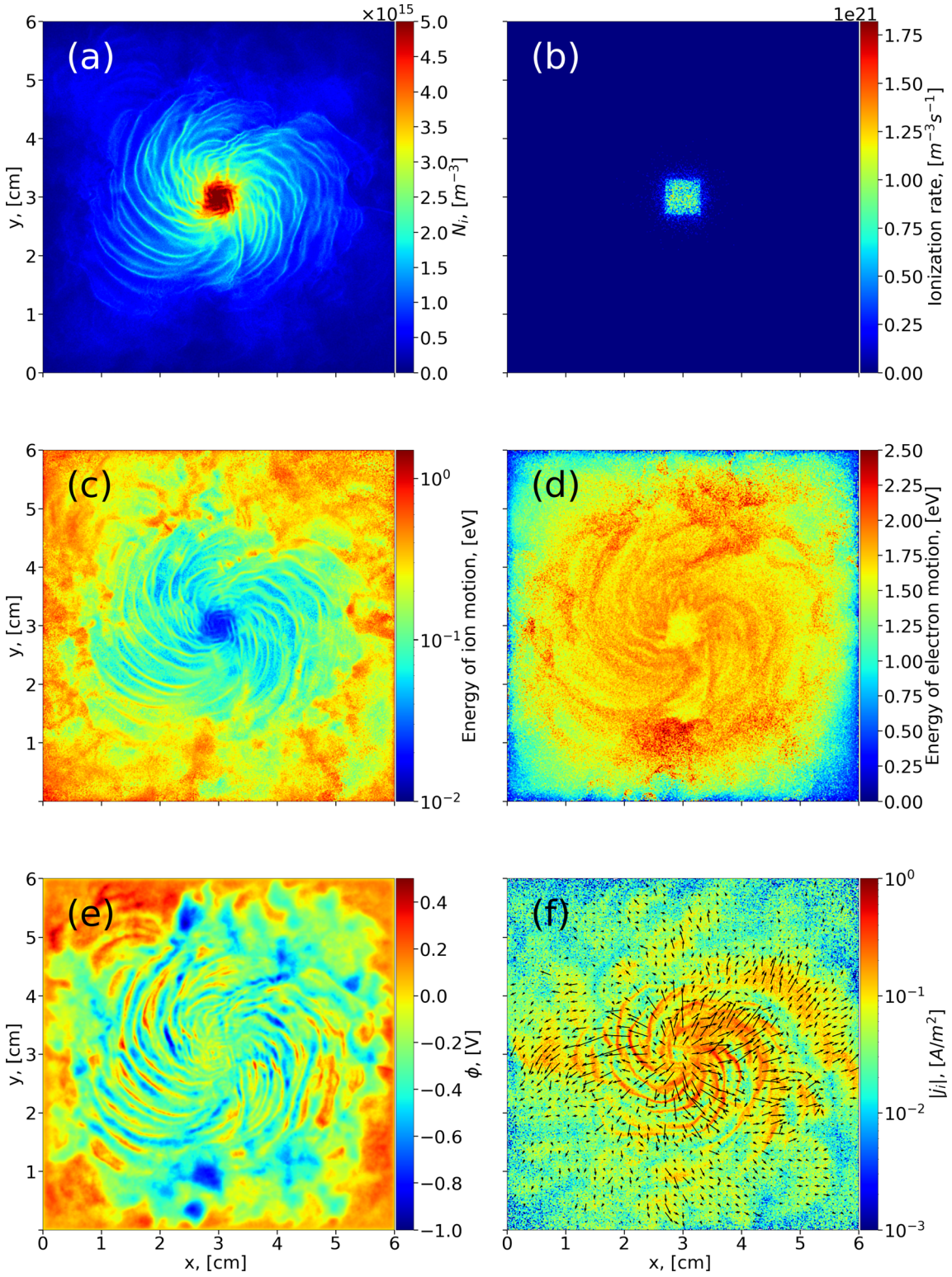

FIG. 20. Snapshots of plasma parameters in the small-scale regime, injection energy 30 eV: (a) ion concentration; (b) ionization rate; (c) ion energy; (d) electron energy; (e) potential; and (f) absolute value of the ion current density with the direction vectors.

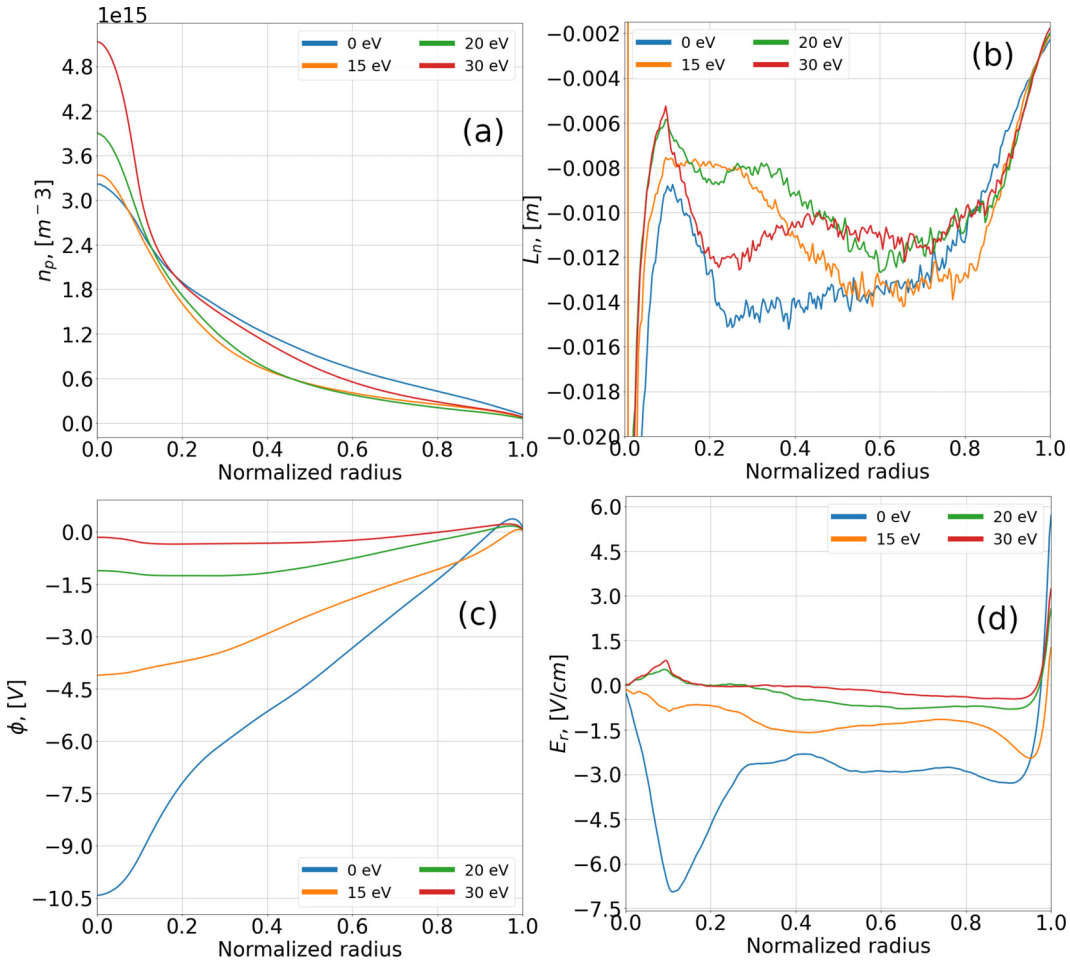

FIG. 21. Radial profiles of plasma parameters in the small-scale regime for different injection energies: (a) ion concentration; (b) gradient scale length; (c) potential; and (d) electric field.

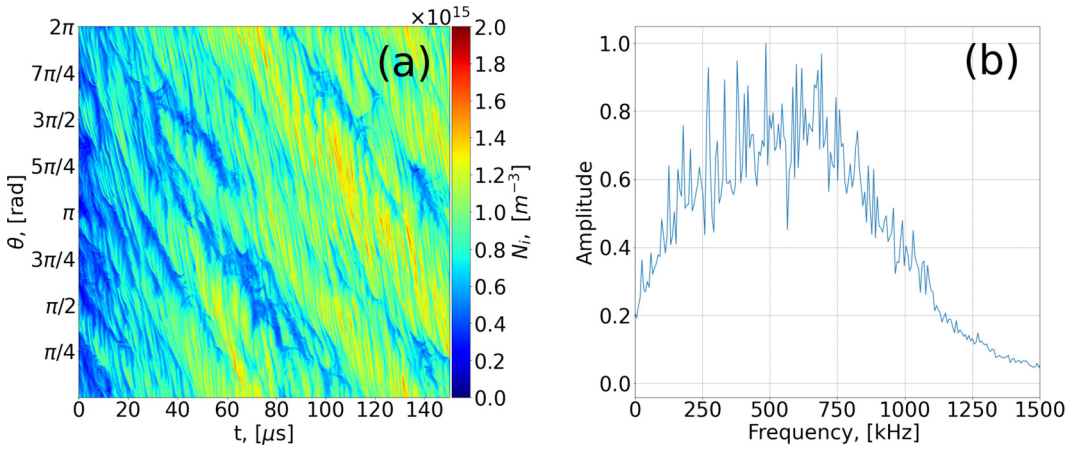

FIG. 22. Fluctuations spectra in the small scale regime: (a) ion density distribution in the $\theta - t$ plane; (b) ion density power spectrum.

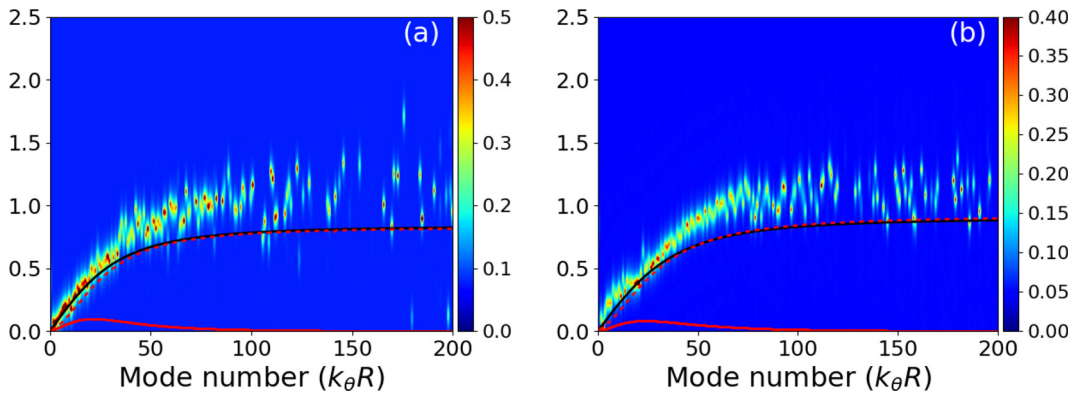

FIG. 23. 1D FFT+MUSIC transform of the space–time data of E_θ. The theoretical real part of the frequency (dashed red) and growth rates (solid red) from the dispersion relation Eq. (3) are plotted to compare with the observed spectra. Black lines show the ion sound frequency: (a) Injection energy = 30 eV; (b) Injection energy = 50 eV.

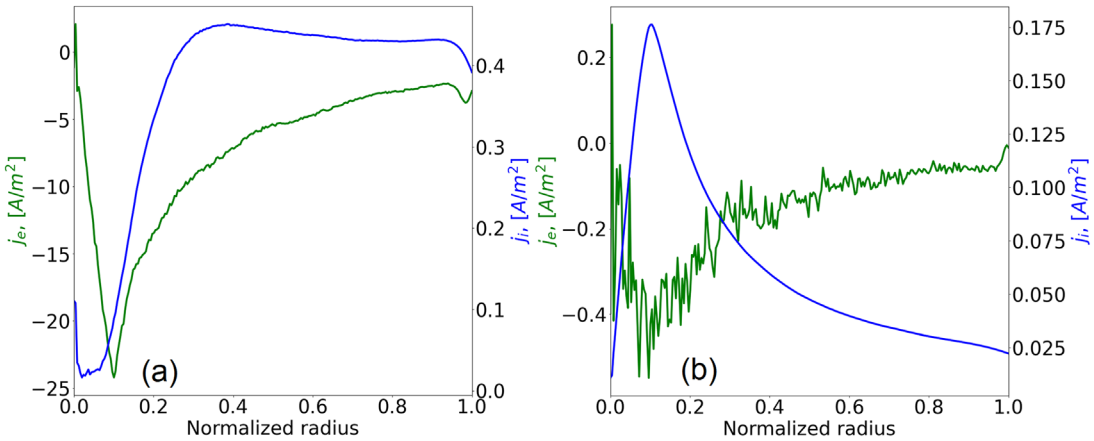

FIG. 24. Electron and ion radial current: a) spoke regime, B = 200 G; b) spiral arms regime, B = 150 G.

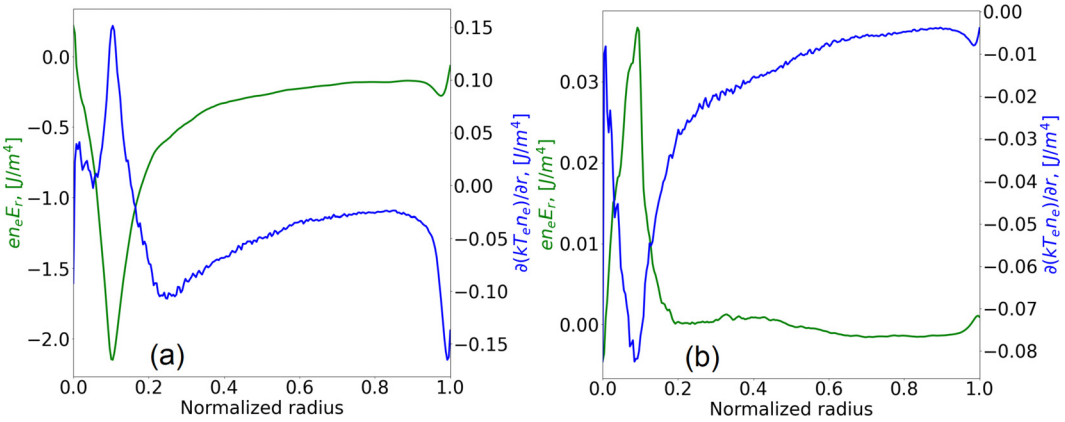

FIG. 25. Relative contributions of the electric field and pressure gradient: (a) spoke regime, B = 200 G; (b) spiral arms regime, B = 150 G.

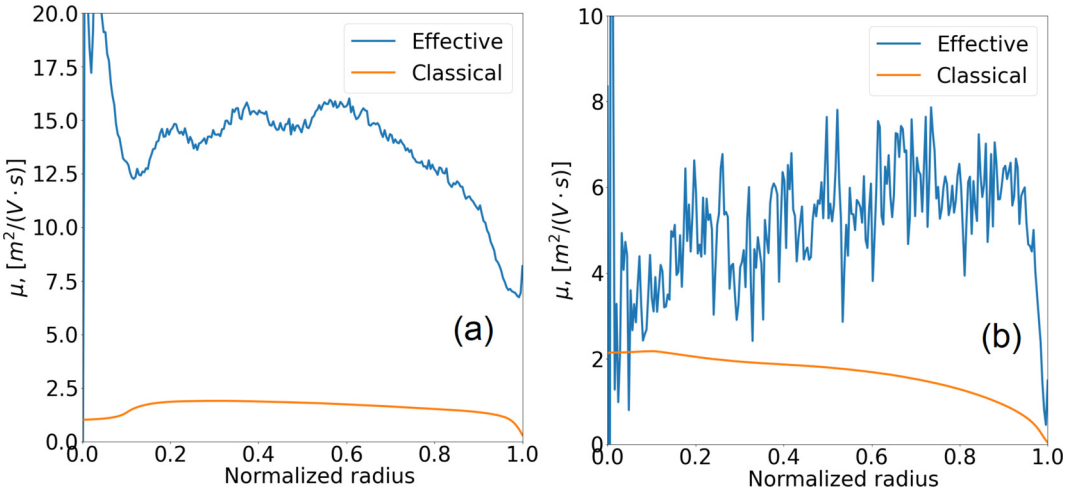

FIG. 26. Anomalous mobility [μ_{eff} from Eq. (7)]: (a) spoke regime, $B = 200$ G; (b) spiral arms regime, $B = 150$ G. Classical mobility is $\mu = e/[m_e\nu(1 + \omega_c^2/\nu^2)]$.

shown that the results are not strongly affected by the difference in the discharge geometry of a similar size. Square, circular, and dodecagon geometry show very similar behavior.

As it was explained above, one of the limitations of the present study is a neglect of ion-neutral collisions and ion losses in the axial direction. This is left for future work.

ACKNOWLEDGMENTS

This work is supported in part by NSERC Canada, U.S. Air Force Office of Scientific Research FA9550–21-1–0031 and Plasma Collaborative Research Facility project at Princeton Plasma Physics Laboratory. The computational resources were provided by Digital Research Alliance of Canada. The authors would like to thank Tech-X for providing the license for Vsim code. The authors acknowledge useful discussions with A. Likhansky.

AUTHOR DECLARATIONS

Conflict of Interest

The authors have no conflicts to disclose.

Author Contributions

Mikhail Sergeevich Tyushev: Data curation (lead); Investigation (lead); Validation (equal); Writing – original draft (equal); Writing – review & editing (equal). **Mina Papahn Zadeh:** Conceptualization (equal); Data curation (supporting); Investigation (supporting); Validation (equal); Writing – original draft (equal); Writing – review & editing (equal). **Vedanth Sharma:** Validation (equal); Writing – original draft (supporting). **Meghraj Sengupta:** Conceptualization (equal); Validation (equal). **Yevgeny Raitses:** Supervision (supporting). **Jean-Pierre Boeuf:** Supervision (supporting); Writing – review & editing (equal). **Andrei I. Smolyakov:** Conceptualization (equal); Funding acquisition (lead); Writing – original draft (equal); Writing – review & editing (equal).

DATA AVAILABILITY

The data that support the findings of this study are available from the corresponding author upon reasonable request.

APPENDIX A: SIMULATION CODES

In this study, we use four PIC codes (EDIPIC, VSim, PEC2PIC, and XOOPIC) to investigate and compare the effect of particle collisions in the Penning discharge supported by the electron beam. The codes are independent and differ in many details, but the main differences are in the way the Poisson equation is solved and the MCC-cross section is calculated. A brief summary of simulation techniques used in each code is provided in (Table VIII).

EDIPIC-2D is a 2D3V-PIC code developed by Sydorenko for the simulation of low-temperature plasmas in electrostatic approximation.[24] Trajectories of charged particles are integrated according to the leap-frog scheme with the Boris algorithm. The Poisson equation is solved using Generalized minimal residual (GMRes) with tolerance 1×10^{-9} using PETSc.[25] The code uses the Monte Carlo method with scattering cross sections of electron-neutral and ionization collision from data from LXcat databases. For Argon—elastic and ionization is from the Hayashi database, www.lxcat.net, retrieved on May 24, 2021, and excitation from the SIGLO database, www.lxcat.net, retrieved on May 24, 2021. For Krypton—Biagi-v7.1 database, www.lxcat.net, retrieved on November 2, 2021. For Nitrogen—BSR-690_N database, www.lxcat.net, retrieved on November 2, 2021. For Hydrogen—Morgan database, www.lxcat.net retrieved on November 11, 2021. It uses the Well Equidistributed Long-period Linear (WELL) algorithm as a pseudo-random number generator.[26]

VSim is a proprietary 3D3V-PIC code developed by Tech-X Corporation for complex multi physics problems. Here, we use it for plasma simulation in the electrostatic setting.[27] VSim uses a Vorpal computation engine and comes up with the VSim composer that provides a graphical user interface. Particle motion is advanced via the leap-frog and Boris schemes. For solving the Poisson equation, the iterative

TABLE VIII. Main features of four PIC codes employed in the benchmarking study.

Code	EDIPIC	VSim	PEC2PIC	XOOPIC
Algorithm				
Particle-Mesh assignment		NA	First order Cloud-in-Cell	
Poisson solver	KSP GMRes (PETSc)	**Iterative:** Generalized minimal residual (GMRes)	**Iterative:** Successive Over Relaxation (SOR)	**Iterative:** Dynamic Alternating Direction Implicit (DADI)
Push solver	**Leap Frog:** Boris Advancement	**Leap Frog:** Boris Advancement	**Lie Operator formalism:** Chin's Exponential Splitting	**Leap Frog:** Boris Advancement
MCC-cross section	**Interpolated** from Lxcat data set	**Interpolated** from **discrete** data set (Lxcat)	**Estimated** from **continuous Regression-based** functions	**Estimated** from **continuous Regression-based** functions
Electron scattering		Anisotropic	Anisotropic	
Hardware acceleration				
Architecture	CPU	CPU	CPU-GPU	CPU
Parallelization	MPI	MPI	Open-MP and Open-ACC	NA
Decomposition	Domain	Domain	NA	NA
Floating-point precision	Double	Double	Double	Double
Language	Fortran 90	C++	Fortran	C++

method of GMRes with tolerance 1×10^{-8} from the Aztec library[28] is used. In VSim, data for cross sections used in the Monte Carlo collision model can be considered either by interpolating the LXcat data set or by specifying the fit function that approximates the cross section. The electron scattering from neutral background follows the anisotropic Vahedi–Surendra algorithm.[29] The ionization cross-section for atomic argon is used from the Morgan database that is updated in 2015, the elastic cross-section is taken from the NIFS-DATA-72 database presented by M. Hayashi which is updated in 2014, and the excitation cross-section is taken from A. V. Phelps report, updated in 2010. For Hydrogen, the cross sections are taken from the Morgan database updated in 2010. Code uses the randOAFunc algorithm which is Vorpal's random number generator.

PEC2PIC is the Parallelized Electrostatic Cartesian 2D Particle-In-Cell 2D3V PIC-MCC solver developed Sengupta and Ganesh.[30,31] PEC2PIC is intended for the device simulations of low temperature

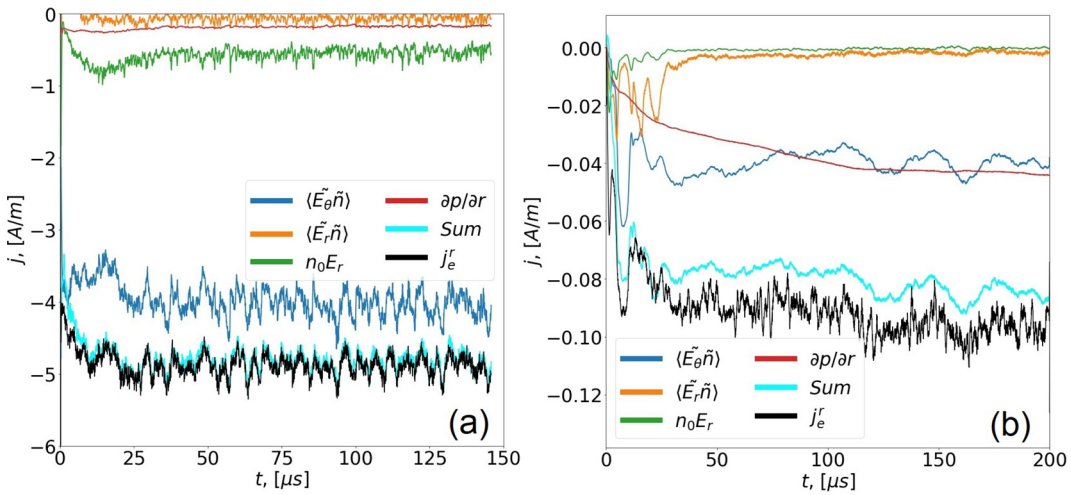

FIG. 27. Relative contributions of different terms in Eq. (8) terms with time: (a) spoke (200 G) and (b) spiral arm (150 G) cases. All terms are averaged over the whole domain. In the case of spiral arms, a moving average was applied to reduce noise.

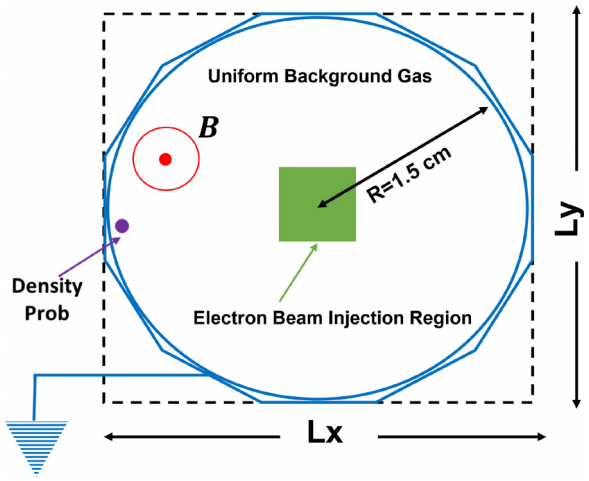

FIG. 28. The end view of the circular cross-section used in VSim and PEC2PIC codes and the dodecagon cross-section that is used in XOOPIC of the modeled discharge.

plasma configurations[32,33] and is part of a larger suite of 1-3D Electrostatic PIC codes PECXPIC developed by Sengupta *et al.*[34] and Khamaru *et al.*[35] PEC2PIC operates on a Cartesian mesh with an iterative Successive Over Relaxation (SOR) Poisson solver,[36] a combination which gives the flexibility to simulate linear as well as curvilinear shapes of Dirichlet boundaries.[37] The Gauss–Seidel solving unit of the SOR is Open-ACC accelerated on a GPU using the red-black parallelization scheme.[38,39] Newtonian dynamics of particle trajectories are solved using the Lie Operator based Chin's exponential splitting integrator.[40,41] Charge interpolation from particle to mesh nodes, and electric field interpolation in the opposite direction are achieved via the first order Cloud-in-Cell (CIC) scheme.[42] The Particle-push and the CIC are parallelized on a CPU node using Open-MP. An MCC routine based on Vahedi *et al.*'s algorithms[29] with an improved electron anisotropic scattering equation[43] simulates the collisional interaction of plasma with background neutrals. The code's language is Fortran and the random generator is Fortran's internal random number generator (xoshiro256**[44]).

XOOPIC (X-windows Object-Oriented Particle In-Cell code) is an open-source 2D3V cartesian (x-y and r-z) software developed by the Plasma Theory and Simulation Group (PTSG).[45] In this work, we use the electrostatic serial version of XOOPIC for non-relativistic equations of motion of charged particles using the Boris advance technique. The Poisson equation is solved by an iterative method of Dynamic Alternating Direction Implicit (DADI) with tolerance 1×10^{-3}. The required cross sections for the Monte Carlo collision are estimated from continuous regression-based functions. For a random generator, Mersenne Twister 19937 generator[46] from the C++ standard library was used.

APPENDIX B: THE EFFECTS OF THE GEOMETRY OF THE SIMULATION REGION

Our base case simulations were performed in the square box geometry, while both rectangular geometry and circular geometry are used in magnetically enhanced $\mathbf{E} \times \mathbf{B}$ discharges.[6] Therefore, it

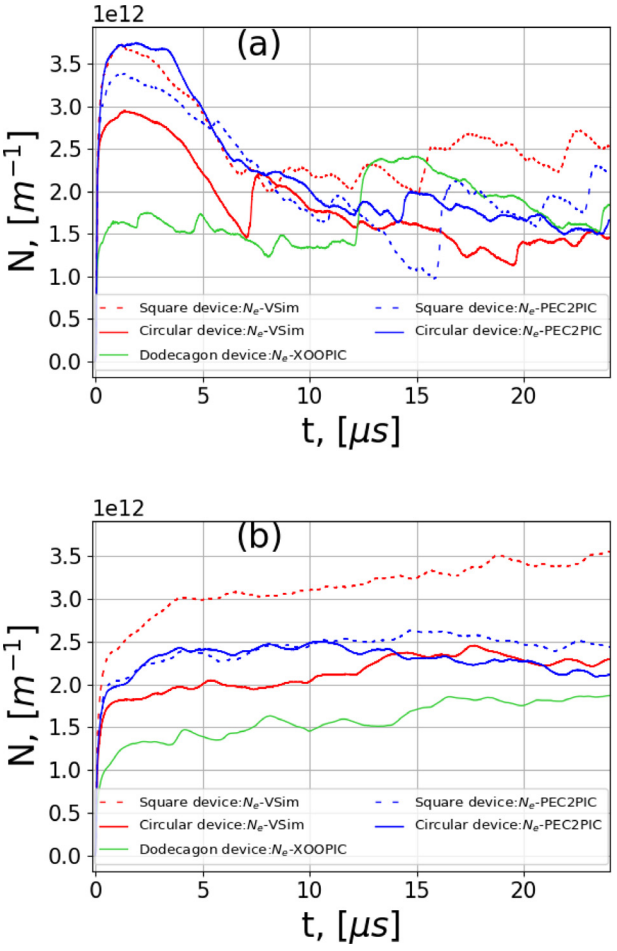

FIG. 29. Temporal evolution of electrons inventory of Argon gas in circular and square simulation geometry. (a) Case with only ionization and (b) case with ionization plus non-ionizing electron neutral collisions. Dashed lines indicate electrons' evolution in square geometry and solid lines show the evolution of electrons in circular-like geometry.

is of interest to investigate the differences that occur for different shapes of the boundary of the simulation region. On this subject, we have performed simulations of the case only ionizing collision and ionization plus non-ionizing electron neutral collisions for Argon and Hydrogen with the circular cross-section implemented in VSim and PEC2PIC codes. In XOOPIC, we have used the dodecagon boundary. Both circular and dodecagon boundaries are located inside the square box of simulation as shown in Fig. 28 with a uniform Cartesian mesh grid. The diameter of the circular is equal to the sides of the square configuration (Fig. 1). The cell size and time step are identical to the corresponding square boundary simulation. Particles are absorbed in cut-cell circular and line segment boundaries (grid-aligned) dodecagon boundaries that conduct the Dirichlet boundary conditions.

Figure 29(a) shows the evolution of electron inventory of Argon discharge simulation with only ionization, in circular and dodecagon devices in comparison with the square devices. It can be

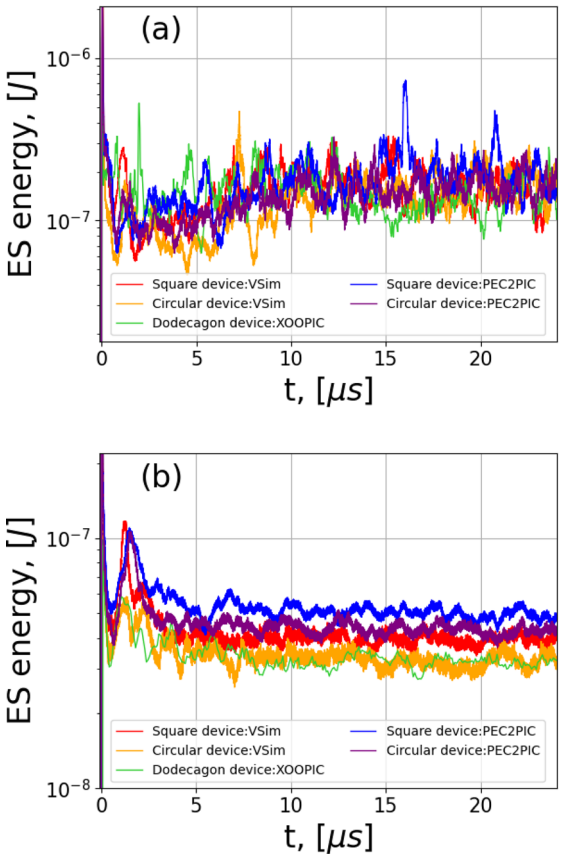

FIG. 30. Temporal evolution of electrostatic energy of Argon gas in circular and square simulation geometry. (a) Case with only ionization and (b) case with ionization plus non-ionizing electron neutral collisions.

seen the number of particles in the saturation level of the circular boundary (solid line) is less than the square boundary (dashed line with similar color). Figure 29(b) which is related to the evolution of electrons in Argon discharge simulation with ionization plus non-ionizing electron neutral collisions, shows a similar result that the number of particles in a circular boundary is less than the corresponding square boundary. The result of simulations of these two cases with dodecagon geometry of XOOPIC code represents good agreement with circular geometry results of VSim and PEC2PIC codes. Figures 30(a) and 30(b) show that the ES energy does not differ for square and circular boundaries at the saturation stage of corresponding simulations.

Figure 31 compares the rotation frequency of the spoke in PEC2PIC simulations of the Argon discharge (with ionizing plus non-ionizing electron–neutral interactions) in square and circular devices. The method used for measuring the $m = 1$ frequency is the same as in Fig. 6 (i.e., density probe signal analysis). Figure 31 (top) shows the smoothened ion density signal of the probe for the two devices while Fig. 31 (bottom) has the corresponding FFT analysis. We get nearly equal spoke rotation frequencies for the devices, indicating the cross-sectional boundary shape has little impact on the steady state spoke's frequency.

Applying Hydrogen gas in simulation case with ionization plus non-ionizing electron neutral collisions, instead of Argon gas, reveals that the main features of simulation results, including particle and ES energy evolution, are not different for square and circular geometries (see Fig. 32). Figure 33 compares the rotation frequency of the spoke in PEC2PIC simulations of the Hydrogen discharge (with ionizing plus non-ionizing electron–neutral interactions) in equal sized square and circular devices. Figure 33 (top) has ion density signals at the probe and Fig. 33 (bottom) has the corresponding FFTs. Unlike Argon, the Hydrogen discharge shows significant differences in the frequency spectrum for the two device shapes. While the $m = 1$

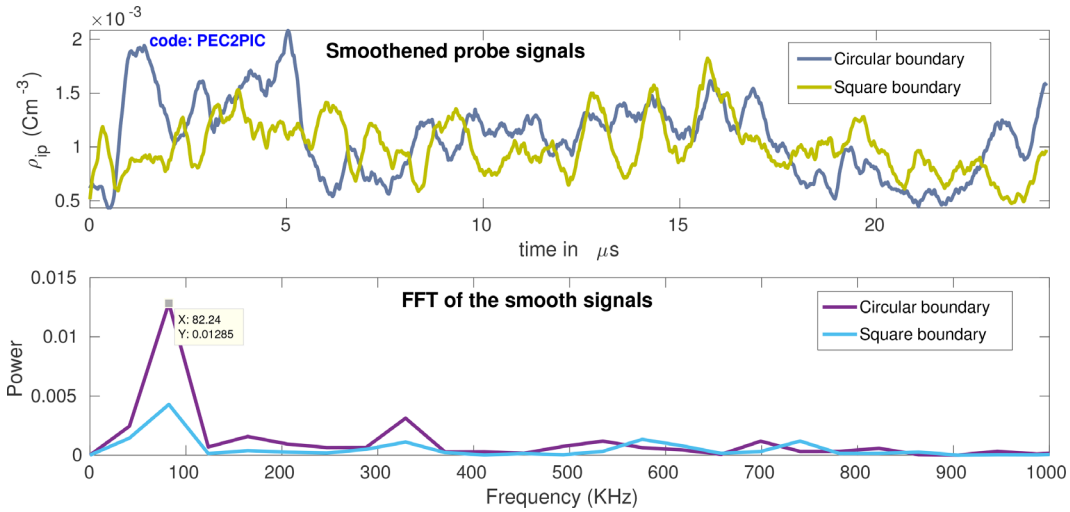

FIG. 31. Comparison of the prob signals for the ion charge density, ρ_{ip}, and power spectrum between square and circle devices for Argon, showing the effect of boundary on spoke frequency.

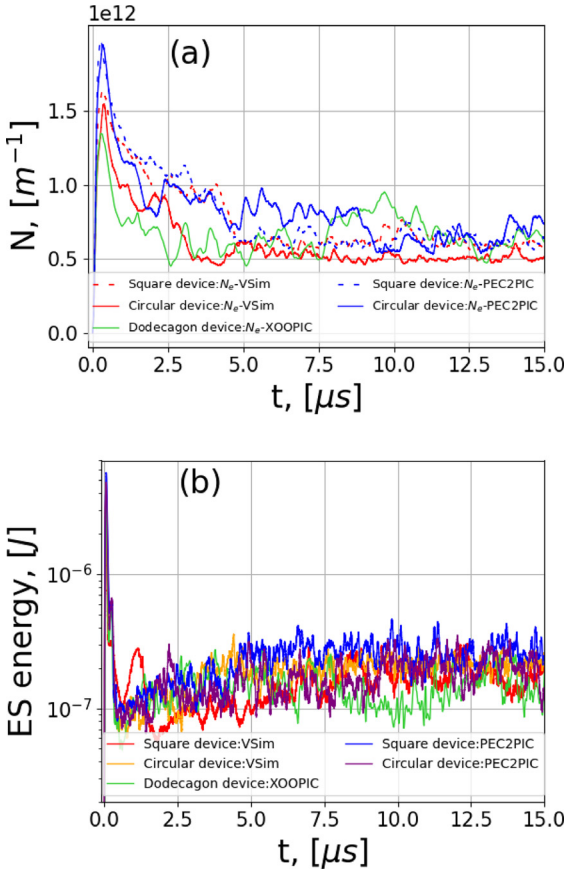

FIG. 32. Temporal evolution of (a) electrons inventory, (b) electrostatic energy of Hydrogen gas for simulation with ionization plus non-ionizing electron neutral collision in circular and square simulation geometry.

frequency for the two configurations is close, about 1.38 MHz the circular device has additional peaks at sub $m=1$ frequencies. The source of these additional peaks needs further investigation to understand.

APPENDIX C: RADIAL CURRENT EQUATION

The conservation of momentum law for electrons without inertia

$$\begin{cases} 0 = -en(E_r + v_\theta B) - \dfrac{\partial p}{\partial r} - \nu m n v_r \\ 0 = -en(E_\theta - v_r B) - \dfrac{1}{r}\dfrac{\partial p}{\partial \theta} - \nu m n v_\theta \end{cases} \tag{C1}$$

expressing v_θ from the second equation and placing it into the first one and neglecting azimuthal pressure gradient (due to cylindrical symmetry) we receive

$$0 = -en\left(E_r - [E_\theta - v_r B]\frac{eB}{\nu_t m}\right) - \frac{\partial p}{\partial r} - \nu_t m n v_r. \tag{C2}$$

Now transferring v_r to the left part of the equation we get

$$v_r n\left[\nu m + \frac{e^2B^2}{\nu_t m}\right] = -en\left(E_r - E_\theta \frac{eB}{\nu m}\right) - \frac{\partial p}{\partial r}. \tag{C3}$$

Multiplying the equation by $-e$ and replacing $\omega_c = \frac{eB}{m}$ and $j_r = env_r$

$$j_r^e = \frac{\nu e^2}{(1+\nu^2/\omega_c^2)\omega_c^2 m_e}\left[nE_r - nE_\theta \frac{\omega_c}{\nu} + \frac{1}{e}\frac{\partial p}{\partial r}\right]. \tag{C4}$$

Now expanding the equation into $n(r,\theta,t) = \tilde{n}(r,\theta,t) + n^0(r,\theta)$, $E_r(r,\theta,t) = \tilde{E}_r(r,\theta,t) + E_r^0(r,\theta)$, $E_\theta(r,\theta,t) = \tilde{E}_\theta(r,\theta,t) + E_\theta^0(r,\theta)$ fluctuation and equilibrium parts, respectively. Also, $\langle n\rangle = n^0$, $\langle E_r\rangle = E_r^0$, and $\langle E_\theta\rangle = E_\theta^0$

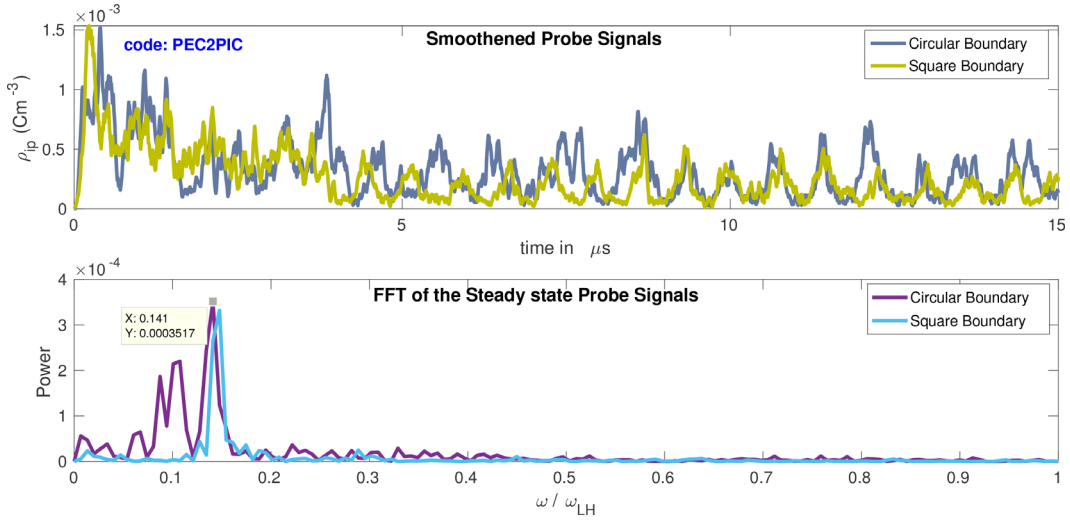

FIG. 33. Comparison of the prob signals for the ion charge density, ρ_{ip}, and power spectrum between square and circle devices for Hydrogen, showing the effect of boundary on spoke frequency.

$$j_r^e = \frac{\nu e^2}{(1+\nu^2/\omega_c^2)\omega_c^2 m_e}\left[n^0 E_r^0 + n^0\tilde{E}_r + \tilde{n}\tilde{E}_r - \left[n^0 E_\theta^0 + n^0\tilde{E}_\theta + \tilde{n}\tilde{E}_\theta\right]\frac{\omega_c}{\nu_t} + \frac{1}{e}\frac{\partial p^0}{\partial r} + \frac{1}{e}\frac{\partial \tilde{p}}{\partial r}\right]. \quad \text{(C5)}$$

After averaging the equation over time we finally achieve

$$j_r^e = \frac{\nu e^2 n^0}{(1+\nu^2/\omega_c^2)m_e\omega_c^2}\left(E_r^0 + \frac{1}{en^0}\frac{\partial p^0}{\partial r}\right) + \frac{e^2\nu}{m_e\omega_c^2}\frac{\langle\tilde{E}_r\tilde{n}\rangle}{1+\nu^2/\omega_c^2} - \frac{e^2}{m_e\omega_c}\frac{\langle\tilde{n}\tilde{E}_\theta\rangle}{1+\nu^2/\omega_c^2}. \quad \text{(C6)}$$

REFERENCES

[1]E. Raitses, I. D. Kaganovich, and A. I. Smolyakov, "Effects of the gas pressure on low frequency oscillations in E × B discharges," in International Electric Propulsion Conference, Hyogo-Kobe, Japan, 4–10 July (2015).

[2]E. Rodriguez, V. Skoutnev, Y. Raitses, A. Powis, I. Kaganovich, and A. Smolyakov, "Boundary-induced effect on the spoke-like activity in $E \times B$ plasma," Phys. Plasmas **26**(5), 053503 (2019).

[3]A. I. Smolyakov, O. Chapurin, W. Frias, O. Koshkarov, I. Romadanov, T. Tang, M. Umansky, Y. Raitses, I. D. Kaganovich, and V. P. Lakhin, "Fluid theory and simulations of instabilities, turbulent transport and coherent structures in partially-magnetized plasmas of **E** × **B** discharges," Plasma Phys. Controlled Fusion **59**(1), 014041 (2017).

[4]S. N. Abolmasov, "Physics and engineering of crossed-field discharge devices," Plasma Sources Sci. Technol. **21**(3), 035006 (2012).

[5]J. Y. Kim, J. Choi, J. Choi, Y. S. Hwang, and K.-J. Chung, "Efficiency improvement of an $E \times B$ Penning discharge source by enhanced cross-field transport of electrons," Plasma Sources Sci. Technol. **31**(5), 05LT02 (2022).

[6]G. Fubiani, G. J. M. Hagelaar, J. P. Boeuf, and S. Kolev, "Modeling a high power fusion plasma reactor-type ion source: Applicability of particle methods," Phys. Plasmas **19**(4), 043506 (2012).

[7]J. P. Boeuf, B. Chaudhury, and L. Garrigues, "Physics of a magnetic filter for negative ion sources—I: Collisional transport across the filter in an ideal, 1D filter," Phys. Plasmas **19**(11), 113509 (2012).

[8]J. P. Boeuf, "Tutorial: Physics and modeling of Hall thrusters," J. Appl. Phys. **121**(1), 011101 (2017).

[9]J. Y. Kim, J. Choi, Y. S. Hwang, and K.-J. Chung, "Electric potential in partially magnetized $E \times B$ discharges," AIP Adv. **11**(8), 085113 (2021).

[10]C. K. Birdsall, "Particle-in-cell charged-particle simulations, plus Monte Carlo collisions with neutral atoms, PIC-MCC," IEEE Trans. Plasma Sci. **19**(2), 65–85 (1991).

[11]Y. Sakawa, C. Joshi, P. K. Kaw, F. F. Chen, and V. K. Jain, "Excitation of the modified Simon-Hoh instability in an electron-beam produced plasma," Phys. Fluids B **5**(6), 1681–1694 (1993).

[12]A. T. Powis, J. A. Carlsson, I. D. Kaganovich, Y. Raitses, and A. Smolyakov, "Scaling of spoke rotation frequency within a Penning discharge," Phys. Plasmas **25**(7), 072110 (2018).

[13]J. Carlsson, I. Kaganovich, A. Powis, Y. Raitses, I. Romadanov, and A. Smolyakov, "Particle-in-cell simulations of anomalous transport in a Penning discharge," Phys. Plasmas **25**(6), 061201 (2018).

[14]R. Gueroult, S. J. Zweben, N. J. Fisch, and J. M. Rax, "**E** × **B** configurations for high-throughput plasma mass separation: An outlook on possibilities and challenges," Phys. Plasmas **26**(4), 043511 (2019).

[15]L. Xu, D. Eremin, and R. P. Brinkmann, "Direct evidence of gradient drift instability being the origin of a rotating spoke in a crossed field plasma," Plasma Sources Sci. Technol. **30**(7), 075013 (2021).

[16]M. H. Hayes, *Statistical Digital Signal Processing and Modeling* (Wiley, 2009).

[17]R. Kleiber, M. Borchardt, A. Könies, and C. Slaby, "Modern methods of signal processing applied to gyrokinetic simulations," Plasma Phys. Controlled Fusion **63**(3), 035017 (2021).

[18]Y. Sakawa, C. Joshi, P. K. Kaw, V. K. Jain, T. W. Johnston, F. F. Chen, and J. M. Dawson, "Nonlinear evolution of the modified Simon-Hoh instability via a cascade of side-band instabilities in a weak beam-plasma system," Phys. Rev. Lett. **69**(1), 85–88 (1992).

[19]R. Gueroult, J. M. Rax, and N. J. Fisch, "Centrifugal instability in the regime of fast rotation," Phys. Plasmas **24**(8), 082102 (2017).

[20]O. Koshkarov, A. Smolyakov, Y. Raitses, and I. Kaganovich, "Self-organization, structures, and anomalous transport in turbulent partially magnetized plasmas with crossed electric and magnetic fields," Phys. Rev. Lett. **122**, 185001 (2019).

[21]V. P. Lakhin, V. I. Ilgisonis, A. I. Smolyakov, and E. A. Sorokina, "Nonlinear excitation of long-wavelength modes in Hall plasmas," Phys. Plasmas **23**(10), 102304 (2016).

[22]N. Brenning, "Review of the CIV phenomenon," Space Sci. Rev. **59**(3–4), 209–314 (1992).

[23]R. Lucken, A. Bourdon, M. A. Lieberman, and P. Chabert, "Instability-enhanced transport in low temperature magnetized plasma," Phys. Plasmas **26**(7), 070702 (2019).

[24]D. Y. Sydorenko, "Particle-in-cell simulations of electron dynamics in low pressure discharges with magnetic fields," Ph.D. thesis (University of Saskatchewan, 2006).

[25]S. Balay, S. Abhyankar, M. F. Adams, S. Benson, J. Brown, P. Brune, K. Buschelman, E. M. Constantinescu, L. Dalcin, A. Dener, V. Eijkhout, J. Faibussowitsch, W. D. Gropp, V. Hapla, T. Isaac, P. Jolivet, D. Karpeev, D. Kaushik, M. G. Knepley, F. Kong, S. Kruger, D. A. May, L. C. McInnes, R. T. Mills, L. Mitchell, T. Munson, J. E. Roman, K. Rupp, P. Sanan, J. Sarich, B. F. Smith, S. Zampini, H. Zhang, H. Zhang, and J. Zhang, see https://petsc.org/ for "PETSc Web Page (2022)."

[26]F. Panneton, P. L'Ecuyer, and M. Matsumoto, "Improved long-period generators based on linear recurrences modulo 2," ACM Trans. Math. Software **32**, 1–16 (2006).

[27]C. Nieter and J. R. Cary, "VORPAL: A versatile plasma simulation code," J. Comput. Phys. **196**(2), 448–473 (2004).

[28]M. A. Heroux, *AztecOO User Guide* (Sandia National Laboratories, 2004).

[29]V. Vahedi and M. Surendra, "A Monte Carlo collision model for the particle-in-cell method: Applications to argon and oxygen discharges," Comput. Phys. Commun. **87**, 179–198 (1995).

[30]M. Sengupta and R. Ganesh, "Linear and nonlinear evolution of the ion resonance instability in cylindrical traps: A numerical study," Phys. Plasmas **22**, 072112 (2015).

[31]M. Sengupta and R. Ganesh, Phys. Plasmas **24**, 032105 (2017).

[32]M. Sengupta and A. Smolyakov, "Mode transitions in nonlinear evolution of the electron drift instability in a 2D annular **E** × **B** system," Phys. Plasmas **27**, 022309 (2020).

[33]M. Sengupta, A. Smolyakov, and Y. Raitses, "Restructuring of rotating spokes in response to changes in the radial electric field and the neutral pressure of a cylindrical magnetron plasma," J. Appl. Phys. **129**, 223302 (2021).

[34]M. Sengupta, S. Khamaru, and R. Ganesh, "Self-organization of pure electron plasma in a partially toroidal magnetic-electrostatic trap: A 3D particle-in-cell simulation," J. Appl. Phys. **130**, 133305 (2021).

[35]S. Khamaru, R. Ganesh, and M. Sengupta, "A novel quiescent quasi-steady state of a toroidal electron plasma," Phys. Plasmas **28**, 042101 (2021).

[36]W. H. Press, B. P. Flannery, S. A. Teukolsky, and W. T. Vetterling, *Numerical Recipes in FORTRAN Example Book: The Art of Scientific Computing* (Cambridge University Press, 1992).

[37]M. Sengupta, "Studies in non-neutral plasmas using particle-in-cell simulations," Ph.D. thesis (HBNI, 2017).

[38]C. Zhang, H. Lan, Y. Ye, and B. D. Estrade, "Parallel SOR iterative algorithms and performance evaluation on a Linux cluster," in Proceedings of the International Conference on Parallel and Distributed Processing Techniques and Applications (PDPTA 2005), Las Vegas, Nevada, June 27–30 (2005), Vol. 1.

[39]L. Olsen-Kettle, *Numerical Solution of Partial Differential Equation*, Lecture Notes at University of Queensland (University of Queensland, Australia, 2011).

[40]S. A. Chin, "Symplectic and energy-conserving algorithms for solving magnetic field trajectories," Phys. Rev. E **77**, 066401 (2008).

[41]S. A. Chin and D. Cator, "The anatomy of Boris type solvers and the lie operator formalism for deriving large time-step magnetic field integrators," arXiv:2109:01901 (2021).

[42]C. K. Birdsall and A. B. Langdon, *Plasma Physics via Computer Simulation* (Taylor and Francis Group, 2004).
[43]A. Okhrimovskyy, A. Bogaerts, and R. Gijbels, "Electron anisotropic scattering in gases: A formula for Monte Carlo simulations," Phys. Rev. E **65**, 037402 (2002).
[44]D. Blackman and S. Vigna, "Scrambled linear pseudorandom number generators," ACM Trans. Math. Softw. **47**(4), 36 (2021).
[45]J. P. Verboncoeur, A. B. Langdon, and N. T. Gladd, "An object-oriented electromagnetic PIC code," Comput. Phys. Commun. **87**(1), 199–211 (1995).
[46]M. Matsumoto and T. Nishimura, "Mersenne twister: A 623-dimensionally equidistributed uniform pseudo-random number generator," ACM Trans. Model. Comput. Simul. **8**(1), 3–30 (1998).